Dislocation-Density Crystalline Plasticity Modelling of Lath Martensitic Microstructures in Steel Alloys

Tarek Hatem, Mohammed Zikry

To cite this version:

Tarek Hatem, Mohammed Zikry. Dislocation-Density Crystalline Plasticity Modelling of Lath Martensitic Microstructures in Steel Alloys. Philosophical Magazine, 2009, 89 (33), pp.3087-3109. 10.1080/14786430903185999 . hal-00529578

HAL Id: hal-00529578
https://hal.science/hal-00529578v1

Submitted on 26 Oct 2010

Dislocation-Density Crystalline Plasticity Modelling of Lath Martensitic Microstructures in Steel Alloys

Journal:	*Philosophical Magazine & Philosophical Magazine Letters*
Manuscript ID:	TPHM-09-Feb-0052.R1
Journal Selection:	Philosophical Magazine
Date Submitted by the Author:	16-Jun-2009
Complete List of Authors:	Hatem, Tarek; North Carolina State University, Mechanical and Aerospace Engineering Zikry, Mohammed; North Carolina State University, Mechanical and Aerospace Engineering
Keywords:	deformation mechanisms, dislocations, finite-element modelling, martensites, martensitic transformations, microstructure, shear bands, steel
Keywords (user supplied):	lath martensite, microstructure, crystal plasticity

Dislocation-Density Crystalline Plasticity Modelling of Lath Martensitic Microstructures in Steel Alloys

T. M. HATEM, and M. A. ZIKRY*†

†Department of Mechanical and Aerospace Engineering, North Carolina State University, Raleigh, North Carolina 27695-7910, USA.

*M. A. Zikry. Email: zikry@eos.ncsu.edu

A three-dimensional multiple-slip dislocation-density-based crystalline formulation, specialized finite-element formulations, and Voronoi tessellations adapted to martensitic orientations, were used to investigate large strain inelastic deformation modes and dislocation-density evolution in martensitic microstructures. The formulation is based on accounting for variant morphologies and orientations, retained austenite, and initial dislocations-densities that are uniquely inherent to martensitic microstructures. The effects of parent austenite orientation and retained austenite were also investigated for heterogeneous f.c.c./b.c.c. crystalline structures. Furthermore, the formulation was used to investigate microstructures mapped directly from SEM/EBSD images of martensitic steel alloys. The analysis indicates that variant morphology and orientations have a direct consequence on dislocation-density accumulation and inelastic localization in martensitic microstructures, and that lath directions, orientations, and arrangements are critical characteristics of high strength martensitic deformation and behaviour.

Keywords: lath martensite; dislocation-densities; finite element; high strength steel; Voronoi tessellation.

1. Introduction

Martensitic microstructures, such as lath, plate, and butterflies, have been commonly observed in several morphologies in steel [1, 2]. These morphologies are generally controlled by alloying elements, such as carbon and nickel. Lath martensitic steels due to their high strength, wear resistance, and toughness have myriad military and civilian applications. These properties are uniquely inherent to martensitic steels, as a result of its lath microstructure that has distinct orientations, distributions, and morphologies pertaining to martensitic transformations, see, for example, [3-16]. Specifically, the effects of lath martensite (b.c.c.) morphology, parent austenite (f.c.c.) orientation, strains related to transformations from f.c.c. to b.c.c. structures, and retained austenite all have interrelated effects on deformation and failure.

Due to the fine microstructure of lath martensite, it has been difficult to fully characterize lath martensite and understand its effect on overall behaviour. Wayman [7-9] conducted a series of pioneering experiments that identified lath martensite's characteristics, such as the habit plane of lath martensite and martensite Orientation Relations (ORs); the lath microstructure in successive layers; the internal and interfacial dislocation microstructure in lath martensite. Kelly [15] utilized Wayman's work to interpret lath martensite microstructure using phenomenological theory to elucidate how martensitic diffusionless transformation occurs. In recent years, Morito and his colleagues [10-14] have conducted significant experiments, utilizing TEM, SEM and EBSD characterization to classify how martensitic structures can be characterized in categories of laths, blocks (variants with low angle mismatch) and packets (collection of blocks with the same habit plane) microstructures and to characterize their orientation relations and distributions. Spanos *et al*. [16] have used EBSD and serial sectioning to construct a 3D morphology of coarse martensite lath, which provided further detailed insights on lath orientations, distributions, and shapes.

Most finite-element investigations pertaining to martensitic steels utilize phenomenological plasticity models, see, for example, [17, 18]. These approaches do not account for the crystalline structure and the inherent anisotropy of martensite. Furthermore, critical martensitic characteristics, such as ORs, morphologies, parent austenite orientations, initial dislocation-densities, and retained austenite are not accounted for in these studies. Molecular dynamic (MD) simulations [19-21] have been invaluable for predicting defect nucleation and transformation at the molecular level. However, there are severe limitations related to temporal and spatial scales that minimize understanding or predicting behaviour at the relevant microstructural level.

Therefore, to address these limitations, we extend the dislocation-density based crystalline models proposed by Zikry and Kao [22] and Ashmawi and Zikry [23] to b.c.c. crystalline microstructures. Within this formulation, we account for martensitic transformations and parent austenite crystalline orientations for an accurate OR description of lath microstructure. This representation is based on arranging variants within packets and blocks that are categorized in terms of habit planes and orientations. Furthermore, the current study accounts for retained austenite and the effects of initial dislocation-densities. An L_∞ Voronoi tessellation algorithm, see [24, 25], is also used to generate physically representative microstructures that have been adapted to account for the orientation of blocks parallel to the habit plane for an accurate representation of martensitic morphologies. These are coupled with specialized finite-element formulations for a predictive framework related to martensitic steels.

This paper is organized as follows: the dislocation-density crystalline plasticity formulation is given in Section 2, the martensitic microstructure representation in terms of orientation, morphology, retained austenite and initial dislocation-density is outlined in Section 3, the computational techniques are given in Section 4, the results are given in Section 5, and a summary of the results is discussed in Section 6.

2. Dislocation-Density Based Multiple-Slip Constitutive Formulation

The formulation for the multiple-slip crystal plasticity rate-dependent constitutive relations, and the derivation of the evolutionary equations for the mobile and immobile dislocation-densities, which are coupled to the multiple-slip crystalline formulation, are outlined here. A detailed formulation is given by Zikry and Kao [22] and Ashmawi and Zikry [23].

It is assumed that the velocity gradient can be decomposed into a symmetric part, the deformation rate tensor, D_{ij} and an anti-symmetric part, the spin tensor, W_{ij}. It is further assumed that the total deformation rate tensor, and the total spin tensor, D_{ij} can be then additively decomposed into elastic and plastic components as

$$D_{ij}=D^{*}_{ij}+D^{P}_{ij}, \qquad W_{ij}=W^{*}_{ij}+W^{P}_{ij} \qquad \text{(1a-b)}$$

in which W_{ij} includes the rigid body spin. The inelastic parts are defined in terms of the crystallographic slip rates as

$$D^{P}_{ij}=P^{(\alpha)}_{ij}*\overset{\bullet}{\gamma}^{(\alpha)}, \qquad W^{P}_{ij}=\omega^{(\alpha)}_{ij}*\overset{\bullet}{\gamma}^{(\alpha)}, \qquad \text{(2a-b)}$$

where α is summed over all slip-systems, and $P^{(\alpha)}_{ij}$ and $\omega^{(\alpha)}_{ij}$ are second order tensors, and are defined in terms of the unit normals to the slip planes and the unit slip vectors to the slip directions.

For rate-dependent inelastic materials, the constitutive description on each slip-system can be characterized by a power law relation as

$$\dot{\gamma}^{(\alpha)}=\dot{\gamma}^{(\alpha)}_{ref}\left[\frac{\tau^{(\alpha)}}{\tau^{(\alpha)}_{ref}}\right]\left[\frac{\left|\tau^{(\alpha)}\right|}{\tau^{(\alpha)}_{ref}}\right]^{\left(\frac{1}{m}\right)-1} \quad \text{no sum on } \alpha, \qquad (3)$$

where $\dot{\gamma}^{(\alpha)}_{ref}$ is the reference shear strain rate which corresponds to a reference shear stress, $\tau^{(\alpha)}_{ref}$ and m is the rate sensitivity parameter. The reference stress that is used here is a modification of widely used classical forms [26] that relate the reference stress to a square root dependence on the dislocation-density as

$$\tau^{(\alpha)}_{ref}=\tau^{(\alpha)}_{y}+Gb\sum_{\xi=1}^{12}a_{\xi}\sqrt{\rho^{(\xi)}_{im}}, \qquad (4)$$

where G is the shear modulus, b is the magnitude of the Burgers vector, $\tau^{(\alpha)}_{y}$ is the static yield stress, and the coefficients, a_{ξ} are interaction coefficients, and generally have a magnitude of unity, and $\rho^{(\zeta)}_{im}$ are the immobile dislocation-densities as defined in the next section.

2.1. The Evolution of Mobile and Immobile Dislocation-Densities

It is assumed that at a given state for a deformed material, the dislocation structure of total dislocation-density, $\rho^{(\alpha)}$, can be assumed to be additively decomposed, into a mobile dislocation-density, $\rho^{(\alpha)}_{m}$, and an immobile dislocation-density $\rho^{(\alpha)}_{im}$ as

$$\rho^{(\alpha)}=\rho^{(\alpha)}_{m}+\rho^{(\alpha)}_{im}. \qquad (5)$$

It is assumed that during an increment of strain, an immobile dislocation-density rate is generated and an immobile dislocation-density rate is annihilated for statistically stored dislocation-densities (see for example, [27]). The balance between dislocation generation and annihilation equations is the basis for the evolution of mobile and immobile dislocation-densities as a function of strain. Based on these arguments, it can be shown [28] \that the coupled set of nonlinear evolutionary equations of mobile and immobile dislocation-densities can then be given by

$$\frac{d\rho_m^{(\alpha)}}{dt} = \dot{\gamma}^{(\alpha)}\left(\frac{g_{sour}}{b^2}\left(\frac{\rho_{im}^{(\alpha)}}{\rho_m^{(\alpha)}}\right) - \frac{g_{\min ter}}{b^2}\exp(-\frac{H}{kT}) - \frac{g_{immob}}{b}\sqrt{\rho_{im}^{(\alpha)}}\right), \qquad (6)$$

$$\frac{d\rho_{im}^{(\alpha)}}{dt} = \dot{\gamma}^{(\alpha)}\left[\frac{g_{minter}}{b^2}\exp\left(-\frac{H}{kT}\right) + \frac{g_{immob}}{b}\sqrt{\rho_{im}^{(\alpha)}} - g_{re\,\mathrm{cov}}\exp\left(-\frac{H}{kT}\right)\rho_{im}^{(\alpha)}\right], \qquad (7)$$

where g_{sour} is a coefficient pertaining to an increase in the mobile dislocation-density due to dislocation sources, g_{minter} is a coefficient related to the trapping of mobile dislocations due to forest intersections, cross-slip around obstacles, or dislocation interactions, g_{recov} is a coefficient related to the rearrangement and annihilation of immobile dislocations, g_{immob} is a coefficient related to the immobilization of mobile dislocations, H is the activation enthalpy, and k is Boltzmann's constant. As these evolutionary equations indicate, the dislocation activities related to recovery and trapping are coupled to thermal activation.

The evolutionary equations are coupled to the multiple-slip crystal plasticity formulation, the four g coefficients in equations (6-7), and the enthalpy, H, must be determined as functions of the deformation mode. The enthalpy, H, is determined by defining an exponential ratio of the current temperature to the reference temperature. The four g coefficients are determined by using the following two general conditions, pertinent to the evolution of dislocation-densities in crystalline materials that the mobile and immobile dislocation-densities saturate at large strains, and that the relaxation of the mobile dislocation-density to a quasi-steady state value occurs much faster than the variation of the immobile density [26, 29, 30].

3. Martensitic Microstructural Representation

The martensitic microstructure has to be accurately represented in terms of orientation, morphology, retained austenite, and transformation dislocation-densities. As experimentally noted by several investigators [3-6], these dominant interrelated four characteristics are needed to account for the martensitic microstructure, since they collectively have a significant interrelated role in understanding and predicting behaviour at different physical scales. The representation of each of these characteristics is outlined in the following subsections.

The austenite phase will be represented as a f.c.c. structure with twelve potential slip-systems with habit planes of {111} and slip directions of <110>, see for example Taylor [31], and Franciosi and Zaoui [32]. The martensitic phase will be represented as (b.c.t./b.c.c. with twenty four potential slip-systems with {110} and {112} slip-planes of for easy and pencil glide, and slip directions of <111>, see, for example, Franciosi [33], Ortiz *et al*. [34].

3.1. Martensitic Orientation

For the crystalline plasticity formulation, the product phase martensite must be related to the global coordinates through a parent austenite grain orientation and variant orientations. Commonly accepted ORs for lath martensitic steels are Kurdjumov-Sachs (K-S) and Nishiyama-Wassermann (N-W) ORs as given by [35].

K-S ORs are based on a γ austenite transformation to an α' martensitic transformation as $(111)_\gamma // (011)_{\alpha'}$, $[\bar{1}01]_\gamma // [\bar{1}\bar{1}1]_{\alpha'}$. For an N-W OR, the transformation is based on $(111)_\gamma // (011)_{\alpha'}$, $[\bar{1}\bar{1}2]_\gamma // [0\bar{1}1]_{\alpha'}$ relation, which is a K-S OR with a 5.12^o degree rotation around the $[011]_\gamma$ direction. Investigations by Wayman [7-9] and Morito [10, 11] have clearly indicated that martensitic steel alloys generally have intermediate ORs that are between K-S and N-W ORs. As can be seen from Table 1, twenty four variants can be obtained for K-S ORs.

A martensitic transformation is a military transformation, where atoms have a fixed relation to each other during the transformation. Martensitic transformations are diffusionless, as it usually occurs at high speed and/or low temperatures, which mandate glissile interfaces between parent and product phases. This interface is the habit plane [35]. The orientation of the habit planes is critical in determining the appropriate martensitic orientations relative to the parent austenite phase. Wayman [9], Kelly [15] and Maki *et al*. [10,11] have identified $(557)_\gamma$ plane as lath martensite's habit plane.

As noted earlier, an essential aspect of representing martensitic texture is to relate the martensitic b.c.c. local grain orientation to the global orientation. Three transformations are needed. The first transformation, $[T]_1$, relates an observed OR to a theoretical OR, such as K-S and N-W ORs. The second transformation, $[T]_2$, relates a martensite OR to the parent austenite grain orientation. The third transformation, $[T]_3$, relates the austenite grain orientation to the global coordinates. These transformations are given by

$$[X]_{Global} = [T]_3 * [T]_2 * [T]_1 * [X]_{\alpha'} \tag{8}$$

Variants are usually deviated from theoretical ORs with random or fixed angles. The first transformation transforms observed martensitic coordinates to a martensitic orientation, such as KS or NW, as

$$[X]_{th\,\alpha'} = [T]_1 * [X]_{Ob\,\alpha'} \tag{9}$$

For example, observed orientations for lath martensite [9-11] can be represented as a misorientation from $[011]_\gamma$ in K-S OR with an angle ϕ, and can be represented as

$$\begin{bmatrix} t/2+c & -s/\sqrt{2} & t/2 \\ s/\sqrt{2} & c & -s/\sqrt{2} \\ t/2 & s/\sqrt{2} & t/2+c \end{bmatrix}, \tag{10}$$

where $s = \sin(\phi)$, $c = \cos(\phi)$, and $t = 1 - \cos(\phi)$, and ϕ generally varies between 0^o and 5.12^o degree for lath martensitic steels.

The second transformation is the theoretical transformation between the product martensitic phase and the parent austenitic phases, such as the KS OR. The second order tensor for the transformation is obtained utilizing the OR for the invariant plane and axis for each variant. A matrix with an orthogonal parallel system of axes can be used for both parent and product phases since $[X]_\gamma = [T]_2 * [X]_\alpha$ and therefore $[T]_2 = [X]_{\alpha'}^{-1} * [X]_\gamma$. For the first variant in Table 1, we have

$$[X]_\gamma=\begin{bmatrix} 1/\sqrt{3} & -1/\sqrt{2} & 1/\sqrt{3} \\ 1/\sqrt{3} & 0 & -2/\sqrt{6} \\ 1/\sqrt{3} & 1/\sqrt{2} & 1/\sqrt{2} \end{bmatrix}, \text{ and } [X]_{\alpha'}=\begin{bmatrix} 0 & -1/\sqrt{3} & 2/\sqrt{6} \\ 1/\sqrt{2} & -1/\sqrt{3} & -1/\sqrt{6} \\ 1/\sqrt{2} & 1/\sqrt{3} & 1/\sqrt{2} \end{bmatrix}, \qquad (11)$$

and,

$$[T]_2=\begin{bmatrix} 0.7416 & 0.6498 & 0.1667 \\ -0.6667 & 0.7416 & 0.0749 \\ -0.0749 & -0.1667 & 0.9832 \end{bmatrix} \qquad (12)$$

Similar transformations can be obtained for all 24 variants related to K-S ORs as presented in Table 1.

The third transformation pertains to the austenite orientation relative to the global axis and the loading directions. Such a transformation is usually represented as three independent Euler angles, where $[T]_3$ can be obtained. Another approach is similar to the approach utilized to obtain $[T]_2$; $[X]_G = [T]_3 * [X]_\gamma$, and $[T]_3 = [X]_\gamma^{-1} * [X]_G$. For example, to align the load with $(111)_\gamma$ and $[-110]_\gamma$, where $[010]_G // [111]_\gamma$, $[001]_G // [-110]_\gamma$, and $[-110]_\gamma \times [111]_\gamma // [100]_G$, the transformation would be

$$[X]_\gamma=\begin{bmatrix} 1/\sqrt{6} & 1/\sqrt{3} & -1/\sqrt{2} \\ -1/\sqrt{6} & 1/\sqrt{3} & 1/\sqrt{2} \\ -2/\sqrt{6} & 1/\sqrt{3} & 0 \end{bmatrix}, \text{ and } [X]_G=\begin{bmatrix} 1 & 0 & 0 \\ 0 & 1 & 0 \\ 0 & 0 & 1 \end{bmatrix}, \qquad (13)$$

then

$$[T]_3=\begin{bmatrix} -0.4083 & -0.4083 & 0.8165 \\ 0.5774 & 0.5774 & 0.5774 \\ -0.7071 & 0.7071 & 0.0 \end{bmatrix}, \qquad (14)$$

and the final transformation to the global axis can be calculated as in equation 8.

3.2. Morphology: Variant Arrangement and Distribution

Another unique characteristic of martensitic microstructure is the fine structure of laths, which are the building cells of the martensitic microstructure. The lath long direction is oriented along $[011]_{\gamma}$, as illustrated in Figure 1. A typical lath geometry is 0.3 x 2.8 x 100 μm [8]. The change in lath width is small relative to the change in the parent austenite grain [14].

To characterize the complex martensitic microstructure that occurs on different length scales, we will follow what Morito *et al.* [10-14] have proposed based on SEM and EBSD characterization. Specifically, we will designate a block as a group of laths with low angle misorientations, and a packet as a collection of blocks with the same habit plane (Figure 2). Blocks will have irregular shapes, although it can be observed that the smallest dimension will be in the direction normal to the habit plane, and block widths can vary between 0.7-8 μm [7, 14]. Using this methodology, we can use the ORs and original austenite orientations to model different variant orientations for different blocks and packets arrangements. Packets can have irregular shapes as well, although the stacking direction of variants is assumed parallel to the habit plane direction. Packet sizes can be approximated as a linear function of prior austenite grain size, and can vary between 0.7-150 μm, see [14] for more details. Due to the microstructural scale that we use in this investigation, the martensitic block is assumed as the smallest scale. Furthermore, as noted by Morito *et al.* [4] martensitic properties are more likely to be related to block size interfacial orientations. In this study, a single parent austenite grain will be considered to further elucidate how grain orientation, packets, and blocks affect mechanical properties and large strain deformation response.

3.3. Retained Austenite

As it is well known, a small amount of retained austenite (approximately 5%) is frequently observed between the martensitic aggregates after the martensitic transformation, see, for example, [5, 7, 36]. In the current study, these effects will be investigated by a random distribution of f.c.c. retained austenite within the b.c.c. aggregate.

3.4. Transformation Dislocations Densities

Martensitic transformation is usually accompanied by large dislocation-densities, see, for example, [13]. These high dislocation-densities are necessary to accommodate the phase transformation and the subsequent glissile interface. Wayman [9] classified the dislocations in martensitic microstructure as two basic types, transformation and interface dislocations. The transformation dislocations are screw dislocation in all four $<111>_{\alpha'}$ direction, with a/2 $[\bar{1}\bar{1}1]_{\alpha'}$ as the dominant direction. Morito *et al.* [13] conducted several experimental studies to characterize the dislocation-densities in nickel and carbon based steels with varying composition. Approximate dislocation-densities of the value of $3.8\text{x}10^{14}$ m^{-2} were obtained for low-nickel lath martensitic steels (Fe-11Ni) [13].

The percentages of mobile to immobile dislocation-densities ratio were not obtained by these studies, as it is difficult to obtain these values experimentally. The initial mobile and immobile dislocations incorporated in the current study were obtained from numerical models based on a proposed transformation crystalline plasticity model [37].

4. Computational Techniques

The total deformation rate tensor, D_{ij}, and the plastic deformation rate tensor, D_{ij}^{P} are needed to update the material stress state. The method used here is the one developed by Zikry

[38] for rate-dependent crystalline plasticity formulations, and only a brief outline will be presented here. An implicit finite element method is used to obtain the total deformation rate tensor, D_{ij}. To overcome numerical instabilities associated with stiffness, a hybrid explicit-implicit method is used to obtain the plastic deformation rate tensor, D_{ij}^{P}. This hybrid numerical scheme is also used to update the evolutionary equations for the mobile and immobile densities.

To physically represent realistic grain shapes, an L_∞ Voronoi tessellation is used. Voronoi tessellations are widely used techniques to generate random grain shapes, as it generates equally distanced boundaries between a random set of points, which can be thought as nucleation sites, see for example [39]. Although, ordinary Voronoi tessellations can be used to generate equilibrium-transformed structures, it may not be appropriate for martensitic steels, since it cannot be used to account for habit plane orientations pertaining to the appropriate martensitic transformation. In this study, L_∞Voronoi algorithms (Hwang [24] and Lee [25]) are used for the representation of martensitic microstructures. The algorithm is based on determining the distances from L_∞ bases, which can be used to orient the blocks along the specified habit planes. The technique can be used to generate orientations around general planes, such as (100) and irrational planes such as (557) by applying needed transformations. Furthermore, smoothing techniques were used to avoid sharp corners along grain and packet interfaces, as illustrated in Figure 3.

5. Results and Discussion

The multiple-slip dislocation-density based crystal plasticity formulation, the specialized finite element algorithm, and the L_∞ Voronoi scheme were used to investigate the large strain inelastic behaviour of martensitic steel. The martensite orientation is represented as outlined in section 3.1. The parent austenite grain is oriented based on the loading plane of $(001)_\gamma$, and two loading directions $[010]_\gamma$ and $[110]_\gamma$. The K-S relation is adopted as the martensite OR, and $\{111\}_\gamma$ is assumed as the habit plane. The martensite morphology is generated by the L_∞ Voronoi tessellation to generate block and packet microstructures relative to the parent austenite grain. A representative aggregate size was determined by modelling the response of aggregates with different aggregate sizes. In this study, 40 martensitic grains are used with 10 packets, with an average of 4 blocks per packet as shown in figure 4. It is assumed that the parent austenite grain has an initial cube orientation.

Using the method outlined by Kameda and Zikry [28], the initial coefficient values, needed for the evolution of the immobile and mobile dislocation-densities given by equations (6-7) were obtained as

$$g_{minter} = 5.53,\ g_{recov} = 6.67,\ g_{immob} = 0.0127,\ g_{sour} = 2.7\text{x}10^{-5},\ \text{and}$$
$$H/K = 3.289\text{x}10^{3}\ {}^{o}\text{K}. \qquad (15)$$

A mobile and immobile dislocation-densities saturation values were obtained for the previous values, and found to be:

$$\rho_{im,s}^{(\alpha)} = 1.16 \times 10^{16}\text{m}^{-2},\ \rho_{m,s}^{(\alpha)} = 6.86 \times 10^{14}\text{m}^{-2}, \qquad (16)$$

To validate the modelling scheme, comparisons were made with experiments conducted by Kumar [40] on 10% Ni steel alloy. Comparisons were made for axial compression strain rates of 0.01/s, and 0.0001/s by applying normal axial loads, with symmetry boundary conditions, as shown in figure 4. Based on a convergence analysis, 2485 four node quadrilateral elements were used with a plane strain analysis for a specimen size of 4.2 mm by 6.3 mm. The material properties (Table 2) that are used here are representative of low nickel alloy steel.

The global nominal stress-strain curve of a comparison between the predictions and the experimental results is shown in figure 5. As seen, there is excellent agreement between the predicted and measured values for both strain-rates for nominal strains up to 30%. These results validate the computational framework and constitutive formulation that has been developed.

As noted earlier, the representation of the morphological martensitic microstructures by tessellation is critical. If ordinary tessellation had been used instead of the adapted L_∞ Voronoi scheme, the results would have been different and inaccurate. Figure 6 compares the results of L_∞ Voronoi and the ordinary Voronoi tessellations with the experimental measurements. Both models have the same set of points and material properties, and the only difference is in the tessellation algorithm. It is clearly obvious that the ordinary Voronoi scheme differs significantly from the experimental results, and that the L_∞ Voronoi has excellent comparison with the experimental measurements. This is due to the incorporation of accurate representations of habit planes, slip-system orientations, and lath long direction within the L_∞ Voronoi scheme. As these microstructural characteristics, as will be seen, have an important effect on deformation and localization.

To further elucidate the local microstructural mechanisms, the contours for the mobile dislocation-densities (figure 7), and the immobile dislocation-densities (figure 8) corresponding to the three most active slip-systems, at a nominal strain of 15% are shown. The maximum normalized (the mobile densities are normalized by the saturated mobile dislocation-density) mobile dislocation-densities are 0.44 for $(\bar{1}12)/[1\bar{1}1]$, 0.22 for $(112)/[11\bar{1}]$, and 0.08 for $(1\bar{1}2)/[\bar{1}11]$. The maximum normalized (the immobile densities are normalized by the saturated immobile dislocation-density) immobile dislocation-densities for the three slip-systems are 0.55 for $(\bar{1}12)/[1\bar{1}1]$, 0.33 for $(112)/[11\bar{1}]$, and 0.17 for $(1\bar{1}2)/[\bar{1}11]$. The evolution of dislocation-densities along selected blocks and along low-angle grain boundaries (as noted earlier grain boundaries are equivalent to block boundaries) result in an increase in dislocation-densities values and a localization of shear slip as shown in figure 9. These increases in dislocation-density are due to an alignment of the load towards $[010]_\gamma$. $[011]_\gamma$ is a maximum resolved shear stress direction for this load, since it is 45^{o} from the loading direction. $[011]_\gamma$ is also parallel to the long direction of laths and blocks, and parallel to the slip direction $[111]_{\alpha'}$ based on the K-S OR.

To further underscore the orientation relation between loading direction, slip-systems, and the lath long directions, the stereographic projection of the slip-systems of variant #11 relative to the loading direction, the locus of maximum resolved shear stress (a circle that is 45^{o} from the loading direction), and the long direction of the variant are plotted as in figure 10. As can be seen, the slip direction $[11\bar{1}]_{\alpha'}$ aligns with $[0\bar{1}\bar{1}]_\gamma$, which is the long direction of the laths inside the block and the maximum resolved shear direction for the uniaxial loading direction of $[010]_\gamma$. Furthermore, slip-plane $(112)_{\alpha'}$ is almost coincident with the maximum resolved shear locus. This would activate slip-system $(112)/[11\bar{1}]$ in this variant as was confirmed by the results shown in figures 6(b) and 7(b).

Similarly for variant #4, the slip direction $[1\bar{1}1]_{\alpha'}$ aligns with the direction $[0\bar{1}1]_{\gamma}$. Slip-plane $(\bar{1}12)$ is nearly adjacent to the maximum resolved shear stress direction. This activates slip-system $(\bar{1}12)/[1\bar{1}1]$ as confirmed by figures 6(a) and 7(a). Similar behaviour can be obtained for other variants. Furthermore, systems $(\bar{1}12)/[1\bar{1}1]$ in variant #4 and $(112)/[11\bar{1}]$ in variant #11 are continuous, which lead to shear-strain localization as shown in figure 9. This special configuration aligns the slip-systems with the maximum resolved shear stress direction with the long direction of the blocks, and when combined with the low angle boundaries between blocks, it acts as shear pipes for the localization of dislocation-densities and shear strains.

As shown in figure 9(a), the accumulated maximum plastic shear is 2.21 at a nominal strain of 15%. This large value is due to geometrical softening and the orientation effects associated with the shear pipes. The geometrical softening occurs due to the large lattice rotation that is high as 31.1^{o} (figure 11(a)), reaching its maximum at the kink on the free surface. The maximum normalized (stress values are normalized by the static yield stress) normal stress is -5.23 (figure 11(b)), and the maximum normalized shear stress is 0.85 (figure 11(c)). These maximum values occur at the blocks boundaries.

It should also be noted that the immobile dislocation-density associated with slip-system $(\bar{1}12)/[1\bar{1}1]$ saturates at a nominal strain of approximately 21%, which is the unloading strain of the experimental specimen. At this strain, several inactive slip-systems are activated due to lattice rotation, and at 30% nominal strain, 21 slip-systems are active through the specimen.

5.1 Parent Austenite Orientation

In this section, we investigate the effects of initial austenite orientation on large strain inelastic deformation in martensitic steels microstructures. For this analysis, we assumed, as before, one austenite grain would result in 40 blocks and 10 packets, and the microstructure is generated by the L_{∞} Voronoi tessellation algorithm using the same set of points used in the previous analyses. The parent austenite grain is oriented based on a loading plane of $(001)_{\gamma}$, and a loading direction of $[110]_{\gamma}$, by applying a transformation angle of 45^{o}. The Euler angles and the relations with the global axes were determined from the previously presented relation, $[T]_3 = [X]_{\gamma}^{-1} * [X]_G$.

The contours for the mobile dislocation-densities (figure 12), and the immobile dislocation-densities (figure 13) corresponding to the two most active slip-systems, at a nominal strain of 15%, are shown. The maximum normalized mobile dislocation-densities for the two slip-systems are 0.11 for $(110)/[1\bar{1}1]$, and 0.08 for $(011)/[\bar{1}11]$, while the maximum normalized immobile dislocation-densities are 0.22 for $(110)/[1\bar{1}1]$, and 0.18 for $(011)/[1\bar{1}1]$. Furthermore, both dislocation-densities and shear slip (figure 14(a)) are uniformly distributed throughout the specimen with no evident of localization. This can be due to the orientation effects of the austenite grain, since the blocks and the lath long directions are inclined, and not coincident, with the maximum shear stress orientation (figure 14(a)). The maximum shear slip is 0.64, which is three times less than the previous model, and the maximum lattice rotation is 30.73^{o} (figure 14(b)).

5.2 Retained Austenite

It has frequently been observed that there are small percentages of retained austenite between laths and blocks in lath martensite, see, for example, [5, 36]. To investigate these effects, we modelled a heterogeneous crystalline structure with f.c.c. for the retained austenite structure and b.c.c. for the martensitic structure. We assumed that 10% of the volume is retained austenite. The retained austenite was assumed to be parallel to the long direction of the blocks in two configurations; inside the martensitic blocks (Model 1), and between blocks/packets (Model 2).

The shear slip and lattice rotation for both models are presented in figure 15. The maximum shear slip is 1.66 for Model 1 and 1.85 for Model 2. The maximum lattice rotation is -30.71° for Model 1 and -34.79° for Model 2. In both cases, there is a considerable decrease in the values of shear slip in comparison with cases with no retained austenite. This difference in behaviour can be due to the interaction of martensitic (b.c.c.) slip-systems with the retained austenitic (f.c.c.) regions. Slip-systems in austenite (f.c.c.) are $\{111\}_{\gamma}/<110>_{\gamma}$, which would be aligned with the $\{110\}_{\alpha'}/<111>_{\alpha}$ based on the KS OR between parent austenite and martenistic systems. However, active slip-systems in the martensitic (b.c.c.), blocks are of the {112} family of planes, which would make it incompatible with f.c.c. slip-systems. This incompatibility between both slip-systems can impede and block dislocation-density transmission and shear-slip accumulation at f.c.c.-b.c.c. interfaces. On the other hand, if we had active slip-systems corresponding to the {110} family of planes, the slip-systems would be compatible with the f.c.c. slip-systems of the retained austenite, and that can enhance plastic strain accumulation and localization.

These results are consistent with experimental observations pertaining to the stabilizing effects of retained austenite, see, for example, [5-6]. Moreover, the proposed approach can be an effective tool in predicting the mechanical behaviour for a wide range of microstructures in steels such as dual phase steels and carbide free bainite steels.

5.4 Physically Representative Microstructure: SEM/EBSD Steel Microstructures

To further validate the proposed approach, the previous models used experimentally SEM/EBSD characterized lath martensite variant orientations and morphologies of low carbon steel (0.2 wt.% C steel), see Kitahara *et al*. [41]. Figure 16, shows the model mapped directly from SEM/EBSD by extrapolating the geometrical coordinates. These images were then discretized into a finite-element mesh.

Figure 17 shows shear slip and lattice rotation at two nominal strains of 5% (a, b) and 15% (c, d). The maximum shear slip is 0.07 at a nominal strain of 5% and 1.92 at nominal strain, of 15% combined with maximum lattice rotation of -2.92 ° at 5% nominal strain and -37.31° at 15% nominal strain. Due to crystal rotations and geometrical softening inside the blocks, the shear slip is highly localized, as seen in figure 17. These results indicate how physical microstructures can be used with the proposed framework to accurately predict behaviour at the relevant martensitic microstructural scale.

6. Summary

This investigation provides detailed validated predictive capabilities that have been used to understand complex interrelated physical mechanisms that relate to martensitic microstructures at different physical scales. A physically based microstructure representation of variants, blocks, packets, retained austenite, and initial dislocations was developed. A multiple-slip rate-dependent crystalline constitutive formulation that is coupled to the evolution of mobile and immobile dislocation-densities, and specialized computational schemes have been developed to investigate the effects of variant shapes, orientations, retained austenite, parent austenite grain orientations, and initial dislocation-densities associated with transformation strains with different orientations relative to the loading direction.

For a loading direction of $[010]_\gamma$, significant increases in dislocation activities occur along the blocks, and slip-systems $(1\bar{1}2)$ / $[\bar{1}11]$, $(\bar{1}12)$ / $[1\bar{1}1]$, and (112) / $[11\bar{1}]$ are the dominant systems. This configuration is almost coincident with the maximum resolved shear stress direction and with the long direction of blocks. When combined with low angle boundaries between blocks it acts as shear pipes that increase the dislocation-densities and shear strains within highly localized regions. This behaviour was also evident for the mapped SEM/EBSD images, where the loading was oriented on the same direction, which is a further indication of the validity of the proposed predictive methodology.

For the $[110]_\gamma$ loading direction, (110) / $[1\bar{1}1]$, and (011) / $[1\bar{1}1]$ are the most active slip-systems. The shear slip is three times less than the previous loading direction. This can be due to the incompatibility between slip directions, the long direction of laths and the maximum resolved shear stresses, where more grain boundaries are available to impede the dislocation transmission between blocks.

The effects of retained austenite on dislocation activities and behaviour of martensitic steels was also investigated by incorporating f.c.c structures (retained austenite) within b.c.c structures (martensitic blocks) The results clearly show the stabilizing effect of retained austenite and crystalline heterogeneities in reducing plastic strains and lattice rotations in critical regions.

This general methodology underscores the importance of accurately representing martensitic microstructure on different microstructural scales. This predictive framework can be used to model other steel phases and alloys, such as bainite and dual phase steels and to potentially control behaviour at the microstructural scale.

Acknowledgments

Support from the Office of Naval Research through Grant N000140510097, is gratefully acknowledged.

7. References

[1] G.B. Olson and W.S. Owen, *Martensite: A Tribute to Morris Cohen*, ASM International, USA, 1992.
[2] K. Otsuka and C.M. Wayman, *Shape Memory Alloys*, Cambridge University Press, Cambridge, 1999.
[3] G. Krauss, Metall. Mater. Trans. A 32B (2001) p. 205.
[4] S. Morito, H. Yoshida, *et al.*, Mater. Sci. Eng A-Struct. 438-40 (2006) p. 237.
[5] G. Thomas, Metall. Trans. A 9A (1978) p. 439.
[6] H. Nakagawa and T. Miyazaki, J. Mater. Sci. 34 (1999) p. 3901.
[7] W. Wasaka and C.M. Wayman, Acta Metall., 29 (1981). p. 973, 991, 1013.
[8] W. Wasaka and C.M. Wayman, Metallography 14 (1981) p. 49.
[9] B.P.J. Sandvik and C.M. Wayman, Metall. Trans. A 14A (1983) p. 809, 823, 835.
[10] S. Morito, X. Huang, *et al.*, Acta Mater. 54 (2006) p. 5323.
[11] S. Morito, H. Tanaka, *et al.*, Acta Mater. 51 (2003) 1789-1799.
[12] S. Morito, I. Kishida and T. Maki, J. Phys. IV France 112 (2003) p. 453.

[13] S. Morito, J. Nishikawa, *et al.*, ISIJ Int. 43(9) (2003) p. 1475.
[14] S. Morito, H. Saito *et al.*, ISIJ Int. 45(1) (2005) p. 91.
[15] P.M. Kelly, Metall. Trans. 33(3) (1992) p. 235.
[16] D. J. Rowenhorst, A. Gupta, C.R. Feng and G. Spanos, Scripta Mater. 55 (2006) p. 11.
[17] C. McVeigh, F. Vernerey, et al., J. Mech. Phys. Solids 55 (2007) p. 225.
[18] J. Zhai, V. Tomar, *et al.*, J. Eng. Mater-T ASME 126 (2004) p. 179.
[19] M. Grujicic and P. Dang, Mater. Sci. Eng A-Struct. 201 (1995) p. 194.
[20] T. Suzuki, M. Shimono, *et al.*, Mater. Sci. Eng A-Struct. 438-440 (2006) p. 95.
[21] Marian J., Wirth B. D., *et al.*, J. Nucl. Mater. 323 (2003) p. 181.
[22] M.A. Zikry, and M. Kao, J. Mech. Phys. Solids 44(11) (1996) p. 1765.
[23] W.M. Ashmawi, and M.A. Zikry, J. Comput.-Aided Mater. Des. 7 (2000) p. 55.
[24] F.K. Hwang, J. Assoc.for Comput. Mach. 26(2) (1979) p. 177.
[25] D.T. Lee, J. Assoc.for Comput. Mach. 27(4) (1980) p. 604.
[26] H. Mughrabi, Mater. Sci. Eng. 85(1-2) (1987) p. 15.
[27] Q. Liu, D.J. Jensen, *et al.*, Acta Mater. 46(16) (1998) p. 5819.
[28] T. Kameda, and M.A. Zikry, Scripta Mater. 38(4) (1996) p. 631.
[29] B. Bay, N. Hansen, *et al.*, Acta Metall. Mater. 40 (1992) p. 205.
[30] N. Hansen, Mater. Sci. Technol. 6 (1990) p. 1039.
[31] G.I. Taylor, Proc. R. Soc. Lond. A 145 (1934) p. 362, 388.
[32] P. Franciosi and A. Zaoui, Acta Metall. 30 (1982) p. 1627.
[33] P. Franciosi, Acta Metall. 31(9) (1983) p. 1331.
[34] L. Stainier, A.M. Cuitino and M. Ortiz, J. Mech. Phys. Solids 50 (2002) p. 1511.
[35] H.K.D.H. Bhadeshia, *Worked examples in the geometry of crystals.* The institute of metals, London, 2001.
[36] J.A. McMahon and G. Thomas, Proceedings of the 3rd International Conference on the Strength of Metals and Alloys, Institution of Metals, London, 1973, p. 180.
[37] T.M. Hatem and M.A Zikry, Scripta Mater., to be submitted (2009).
[38] M.A. Zikry, Comput. Struct. 50 (1994) p. 337.
[39] S. Torquato, Random heterogeneous materials: Microstructure and Macroscopic Properties, Springer, New York, 2002.
[40] P.Wang, K.S. Kumar, Mater. Sci. Eng. A (2009), in press.
[41] H. Kitahara, R. Ueji, *et al.*, Acta Mater. 54 (2006) p. 1279.

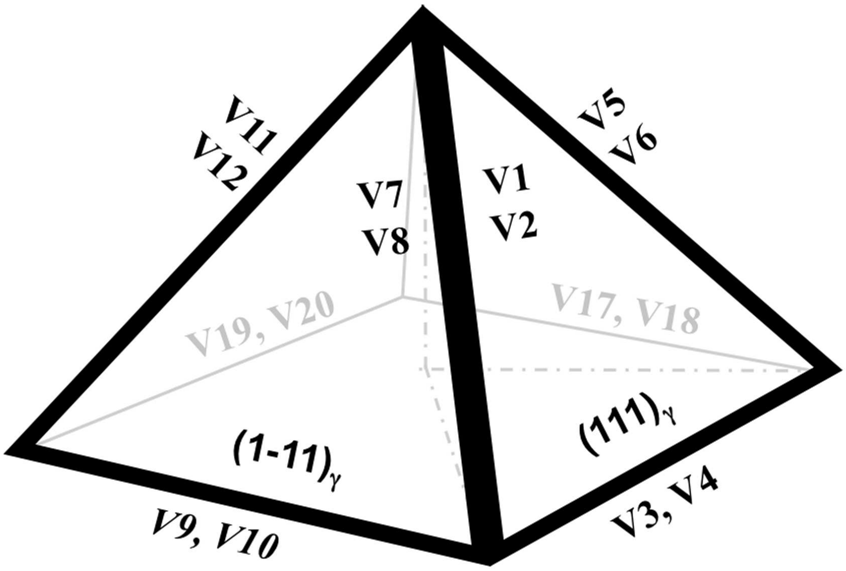

Fig 1
83x62mm (600 x 600 DPI)

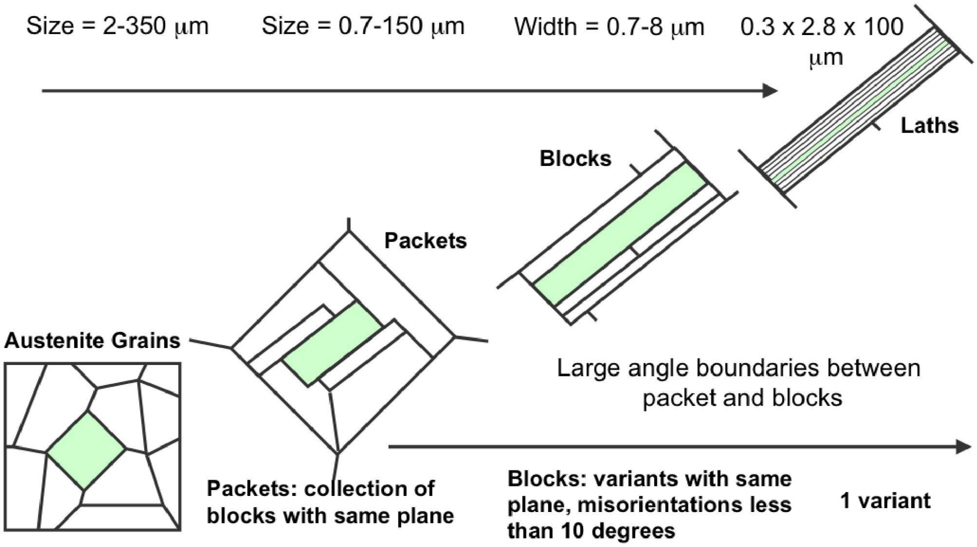

Fig 2
173x130mm (600 x 600 DPI)

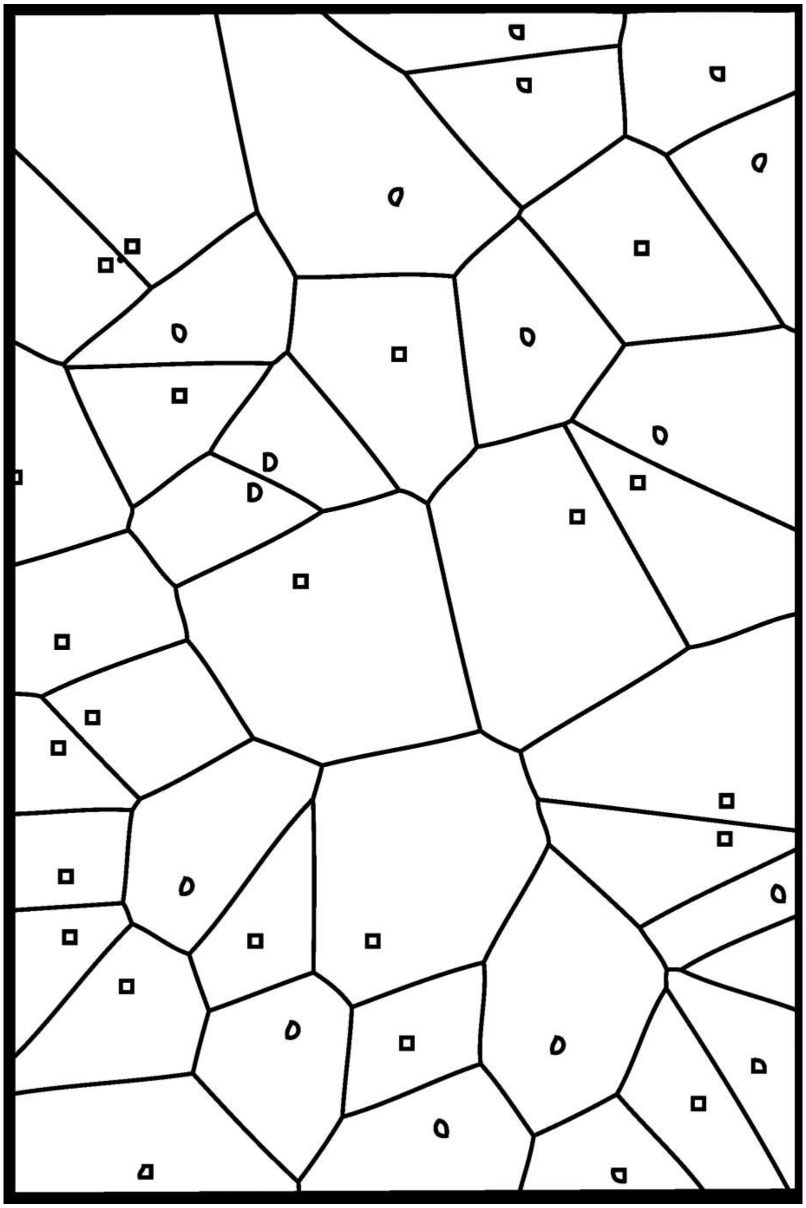

Fig 3a
38x58mm (600 x 600 DPI)

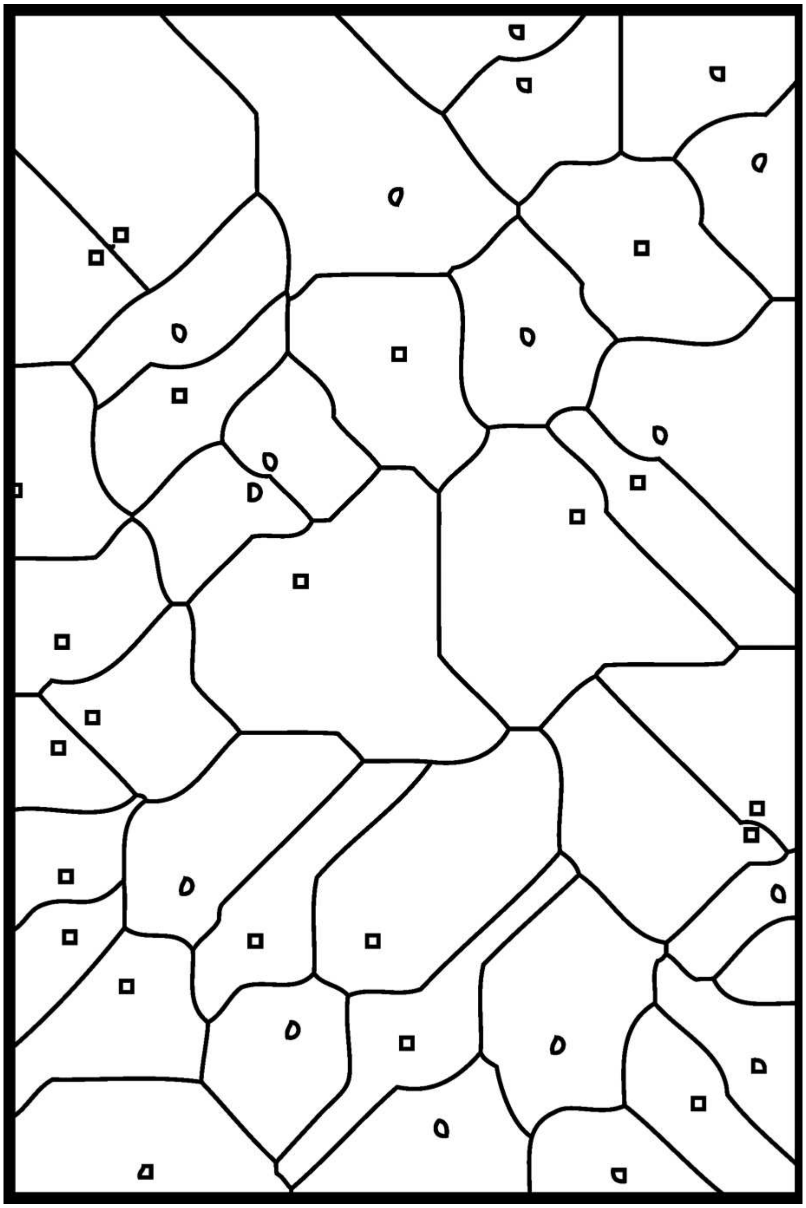

Fig 3b
38x58mm (600 x 600 DPI)

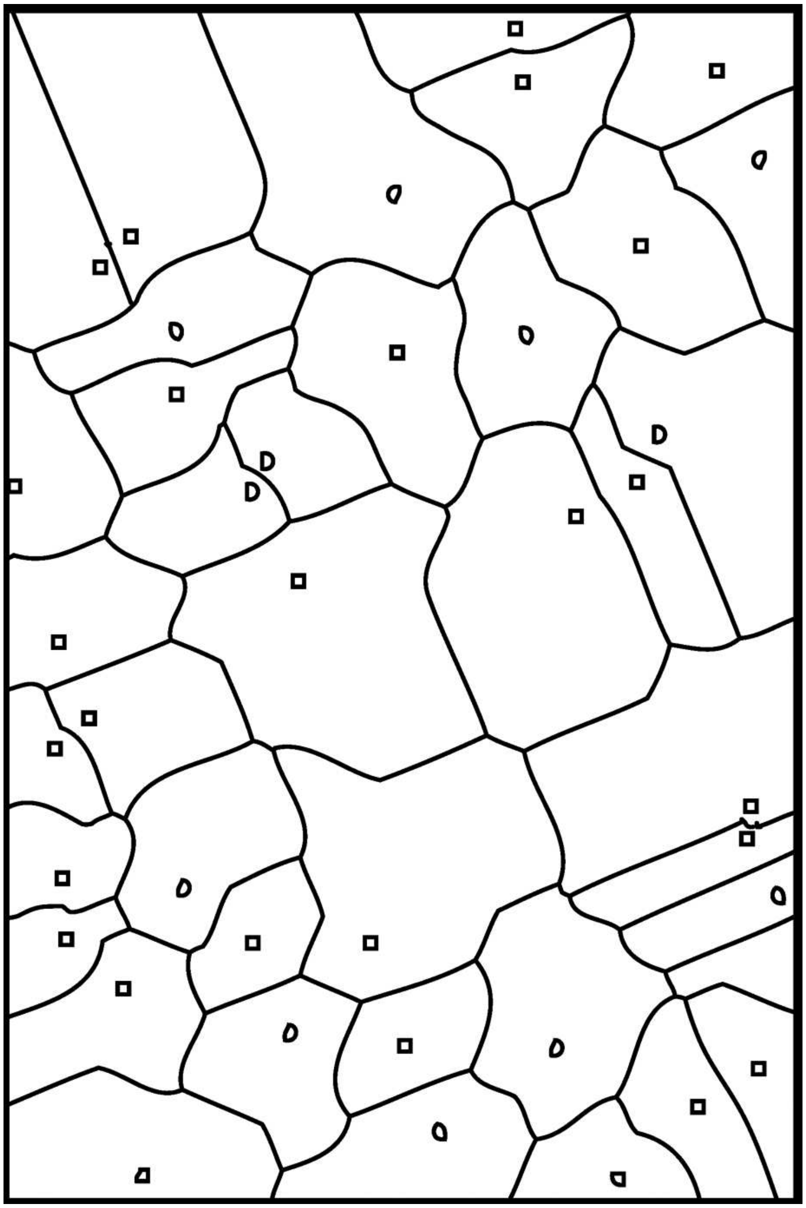

Fig 3c
38x58mm (600 x 600 DPI)

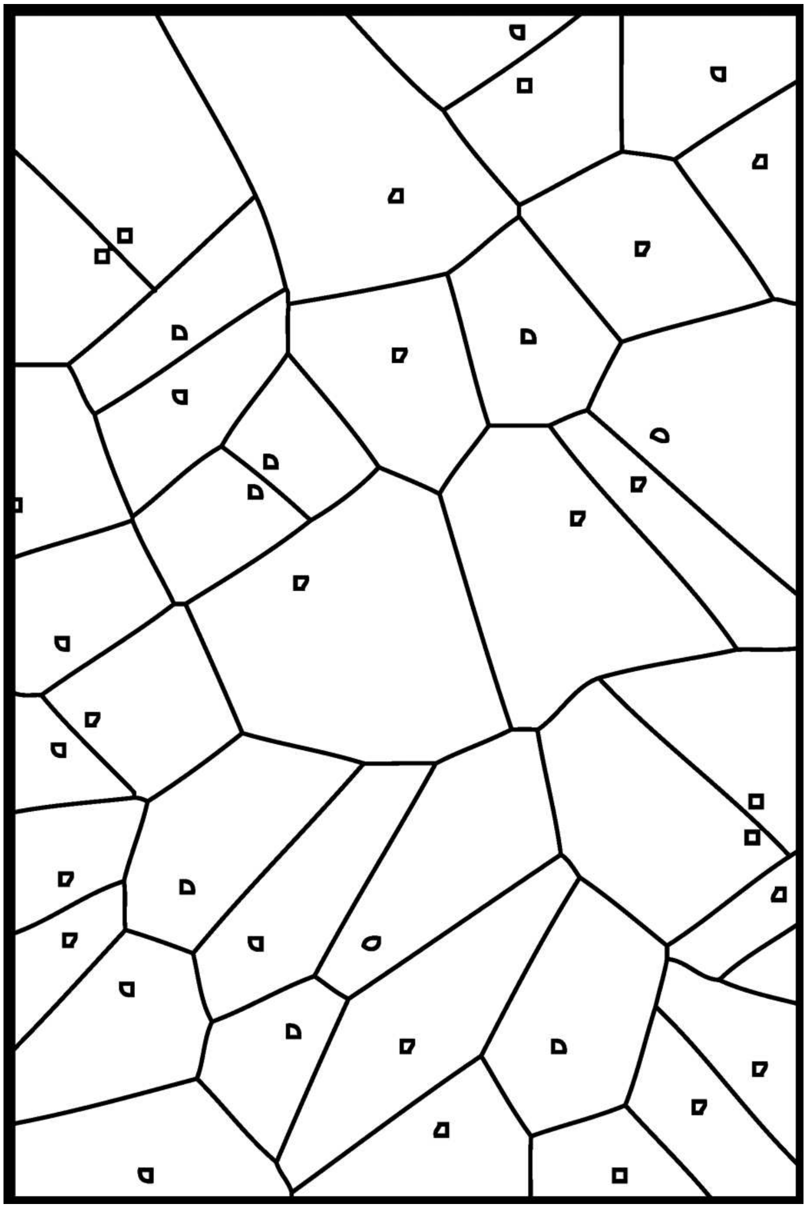

Fig 3d
38x58mm (600 x 600 DPI)

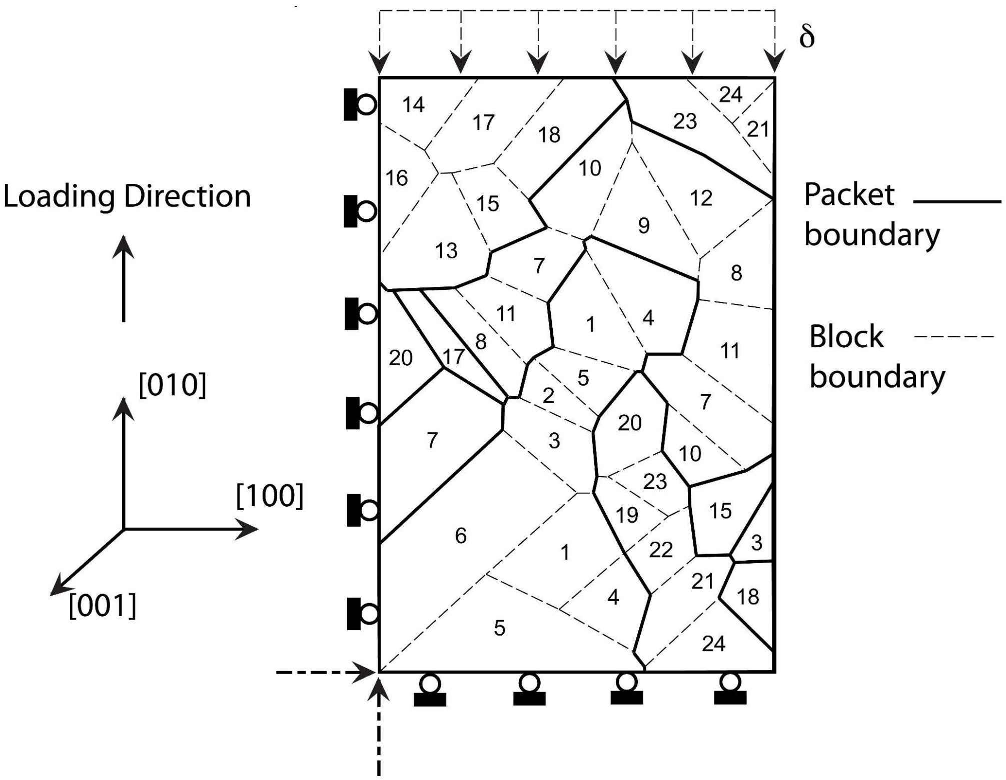

Fig 4
173x134mm (600 x 600 DPI)

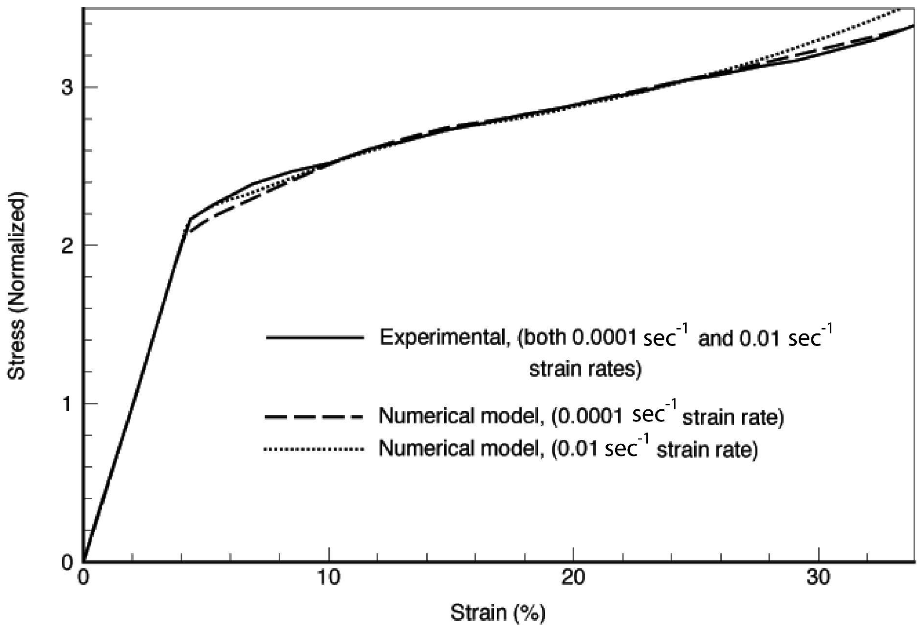

Fig 5
173x125mm (600 x 600 DPI)

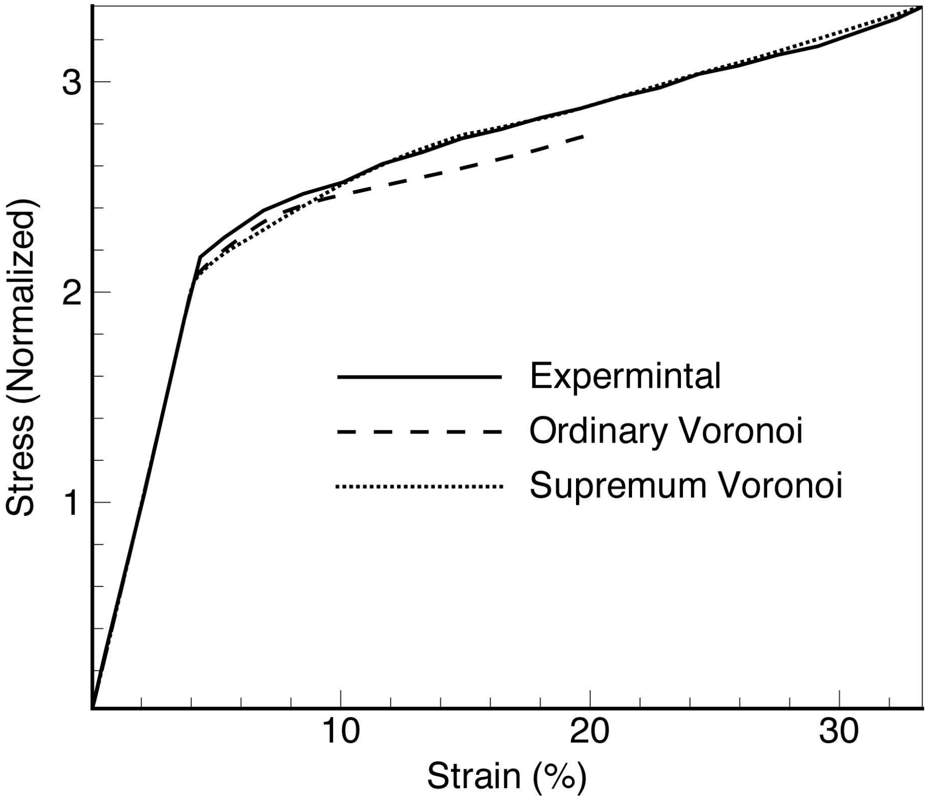

Fig 6
83x76mm (600 x 600 DPI)

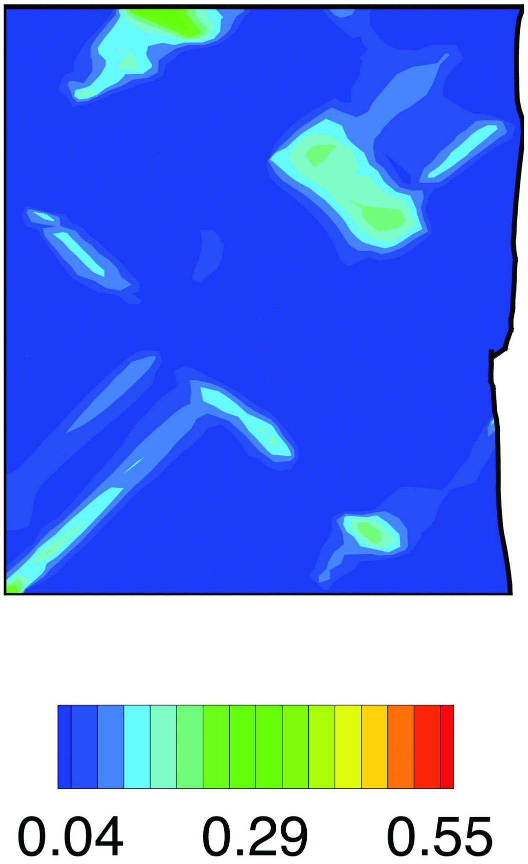

Fig 7a
73x134mm (600 x 600 DPI)

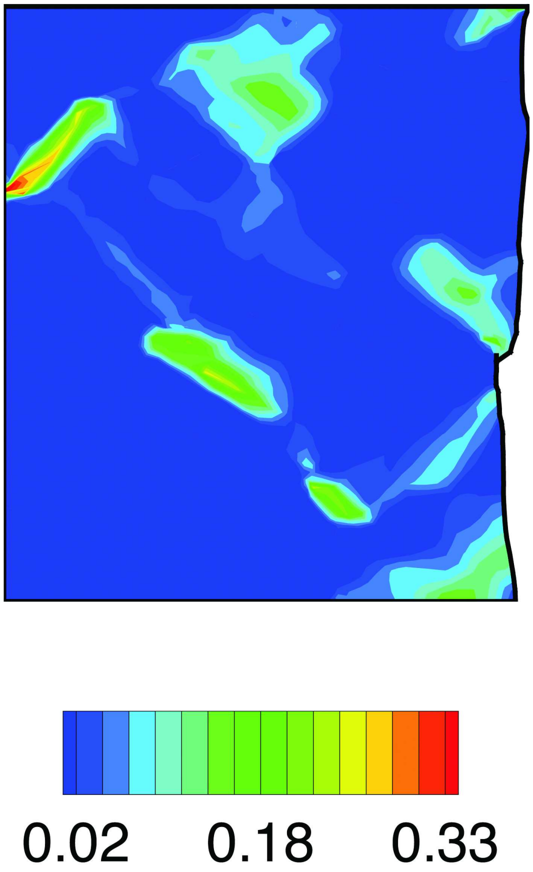

Fig 7b
73x134mm (600 x 600 DPI)

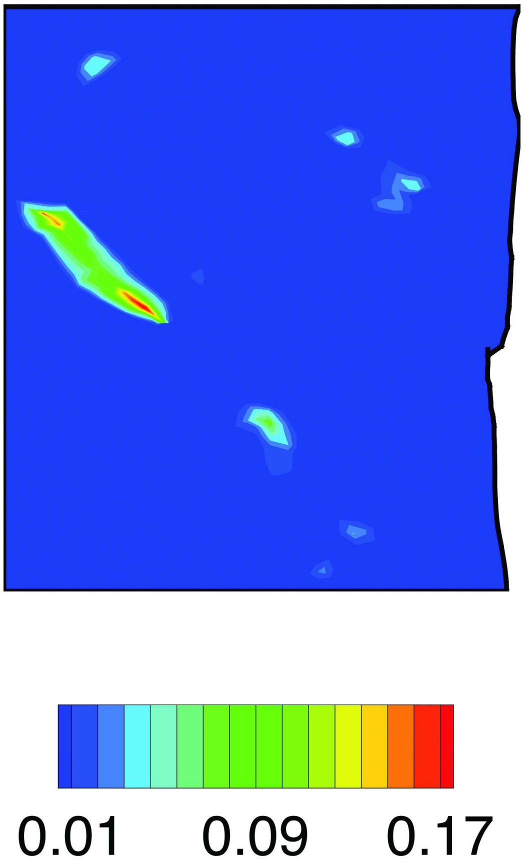

Fig 7c
73x134mm (600 x 600 DPI)

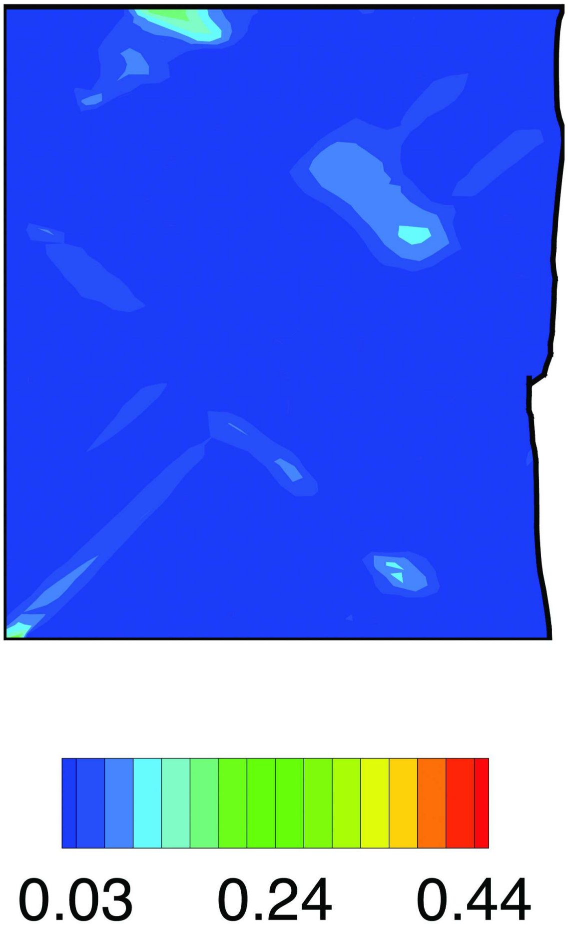

Fig 8a
73x125mm (600 x 600 DPI)

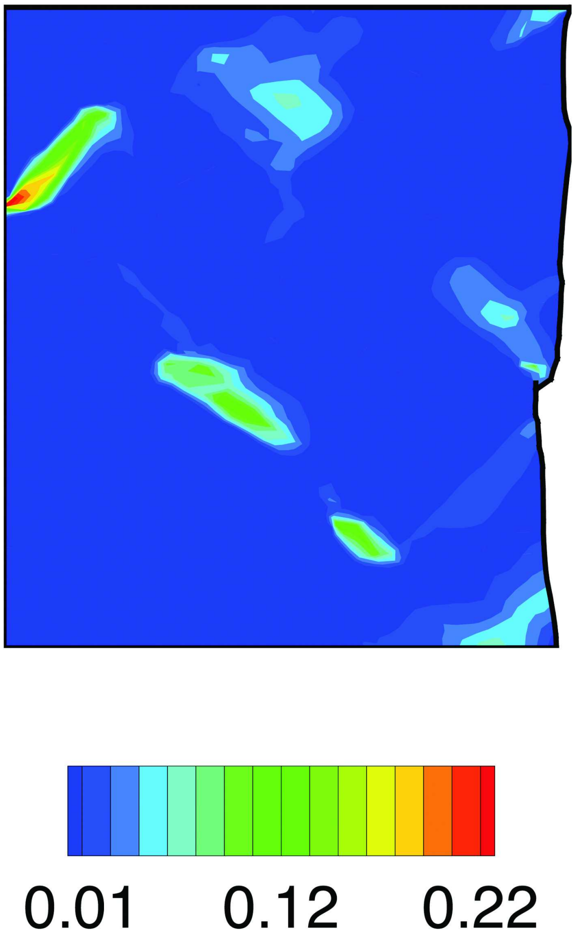

Fig 8b
73x125mm (600 x 600 DPI)

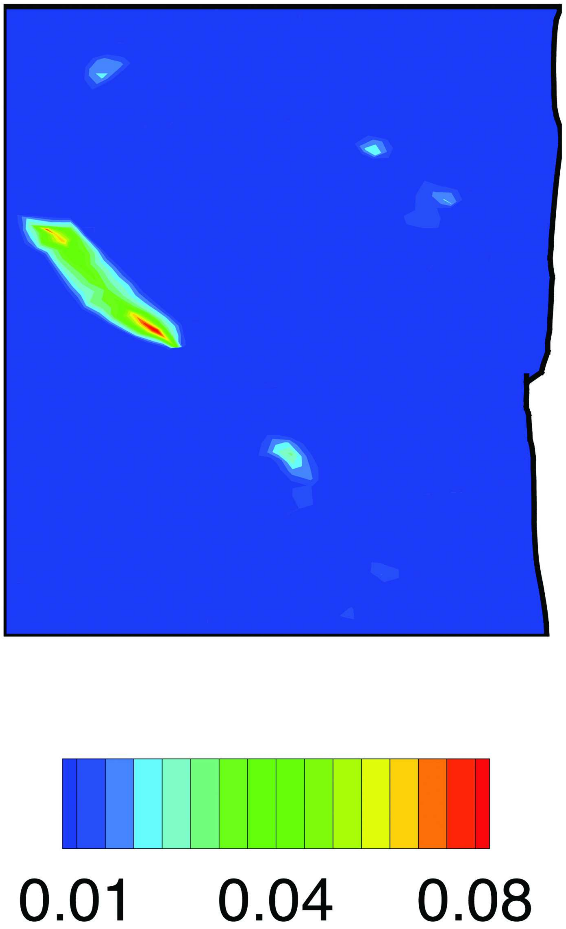

Fig 8c
73x125mm (600 x 600 DPI)

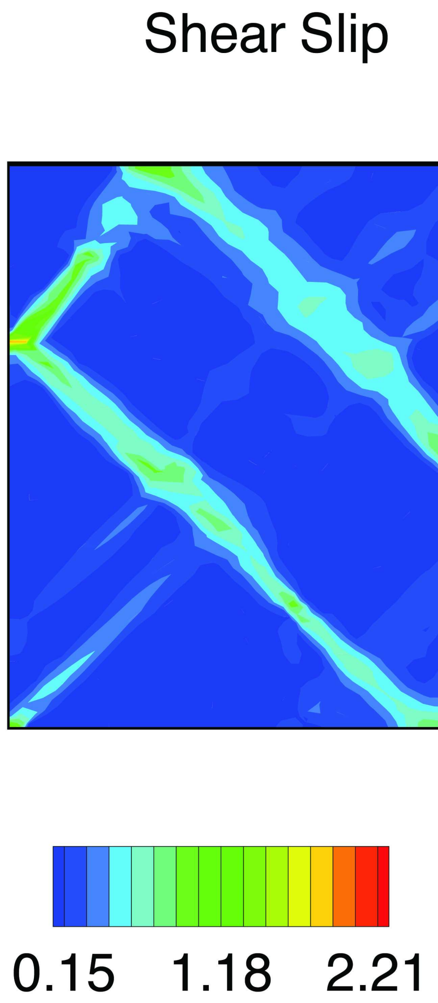

Fig 9a
83x150mm (600 x 600 DPI)

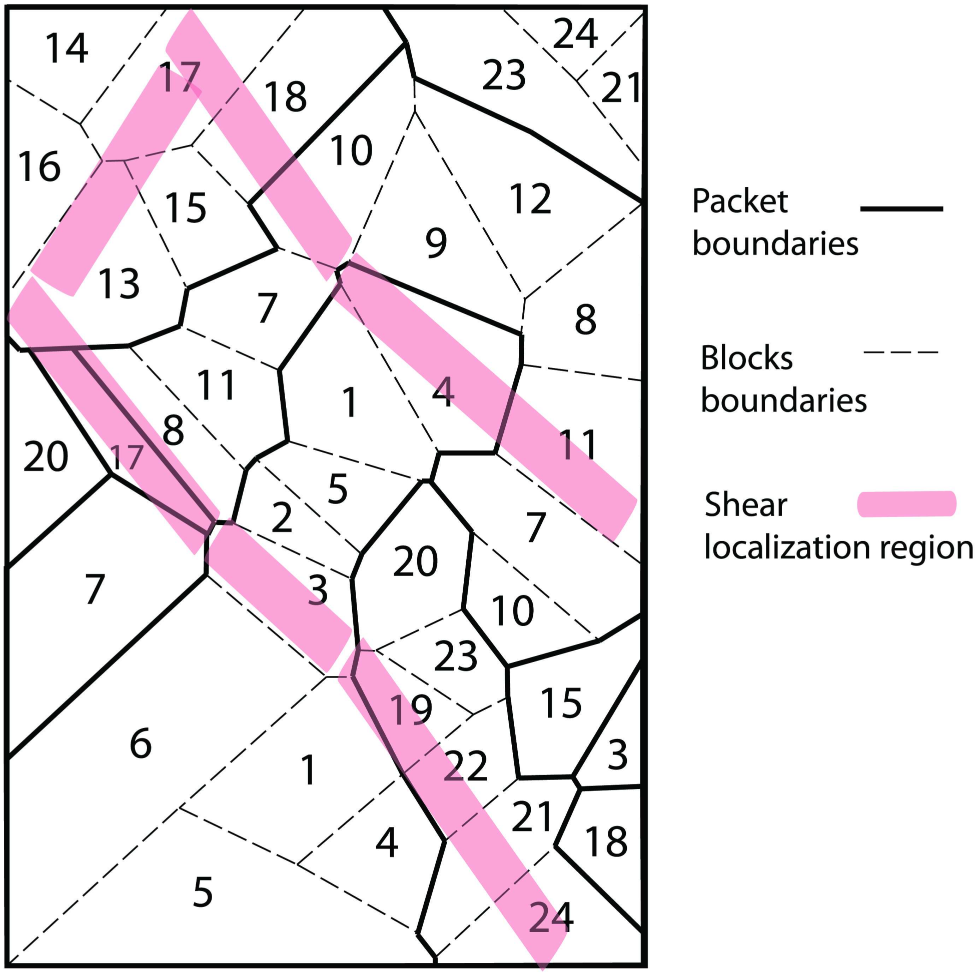

Fig 9b
120x117mm (600 x 600 DPI)

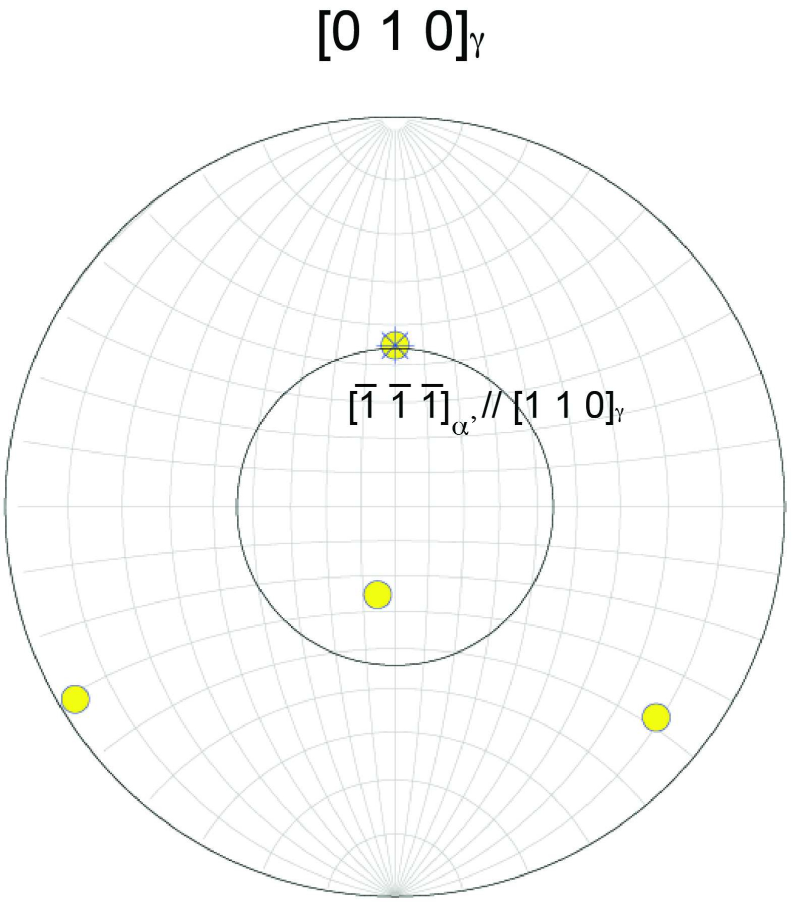

Fig 10a
83x83mm (600 x 600 DPI)

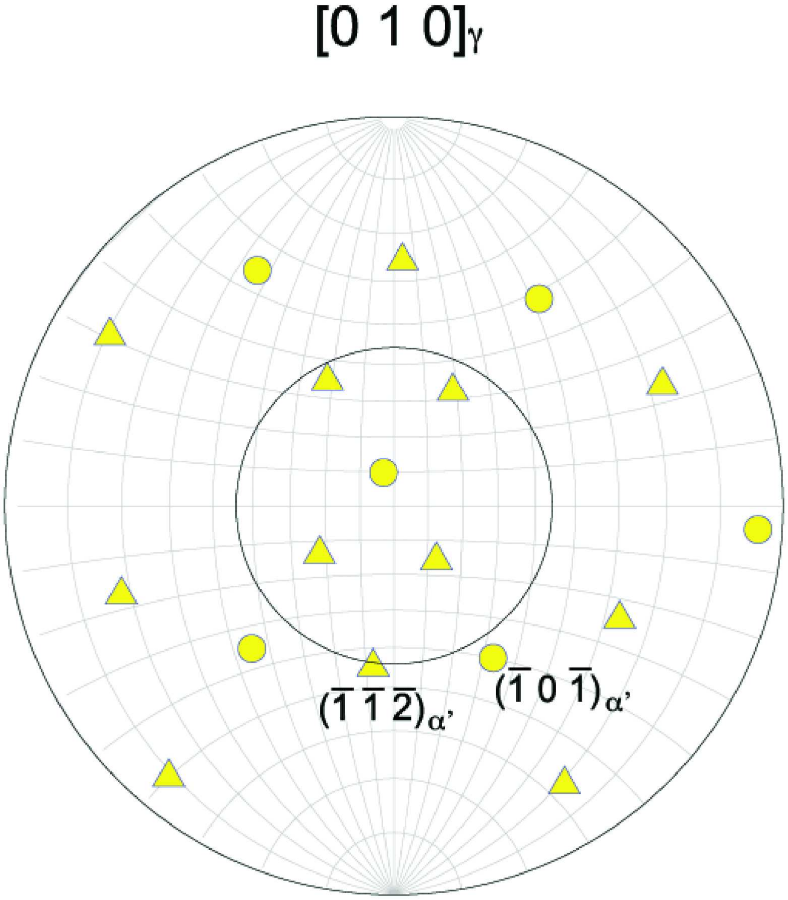

Fig 10b
83x83mm (600 x 600 DPI)

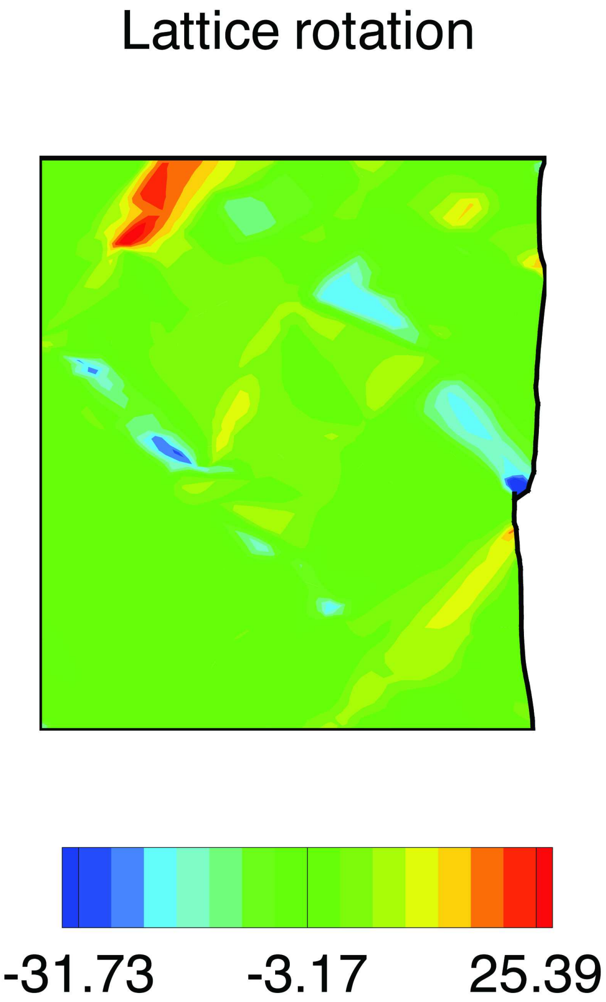

Fig 11a
73x132mm (600 x 600 DPI)

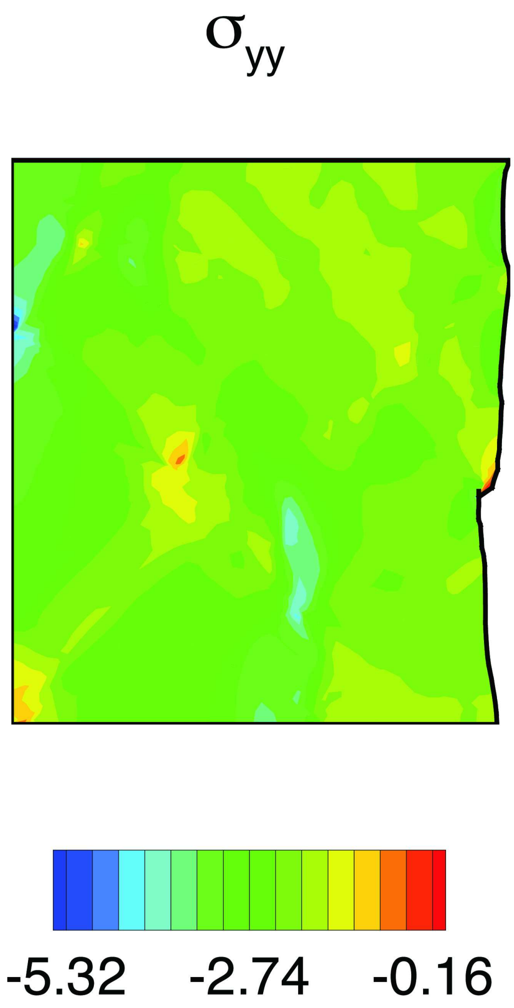

Fig 11b
73x132mm (600 x 600 DPI)

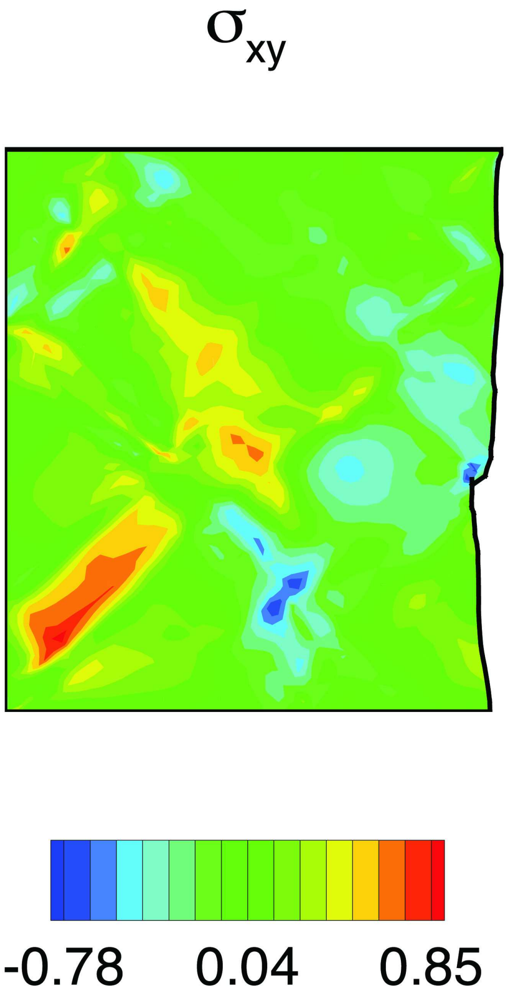

Fig 11c
73x132mm (600 x 600 DPI)

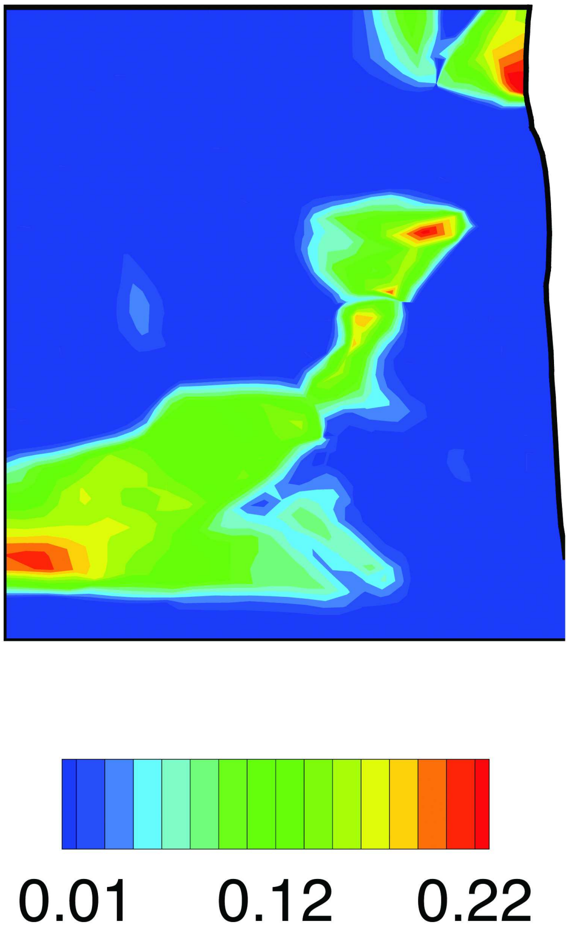

Fig 12a
83x134mm (600 x 600 DPI)

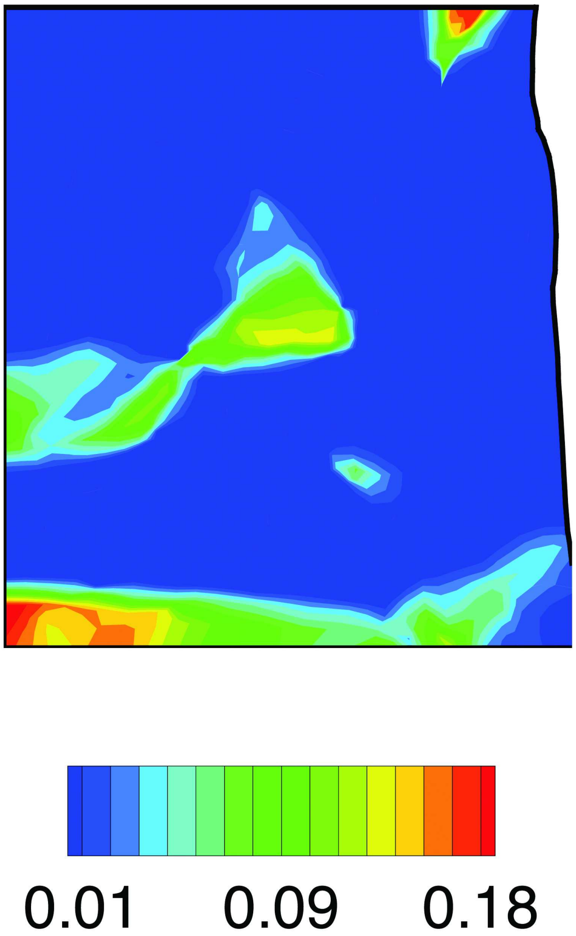

Fig 12b
83x134mm (600 x 600 DPI)

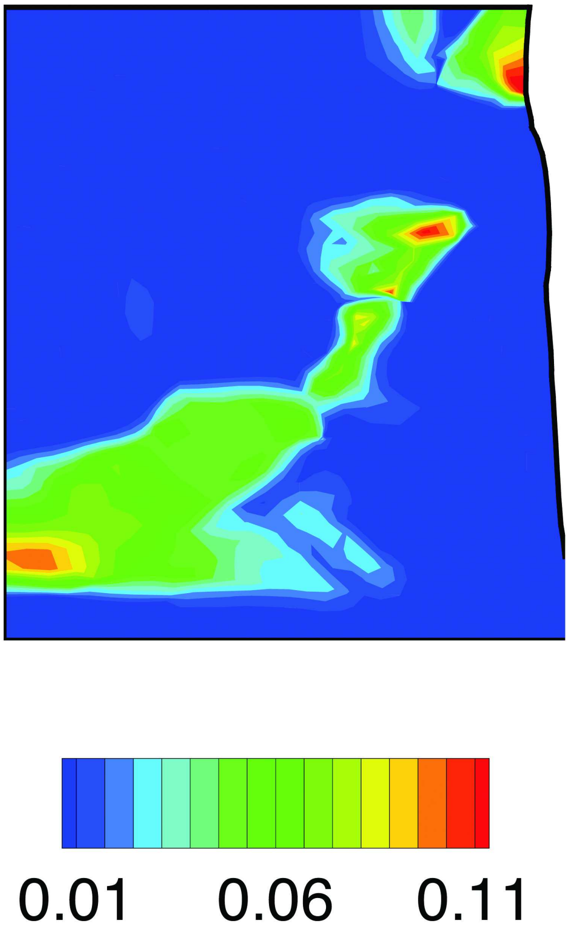

Fig 13a
83x134mm (600 x 600 DPI)

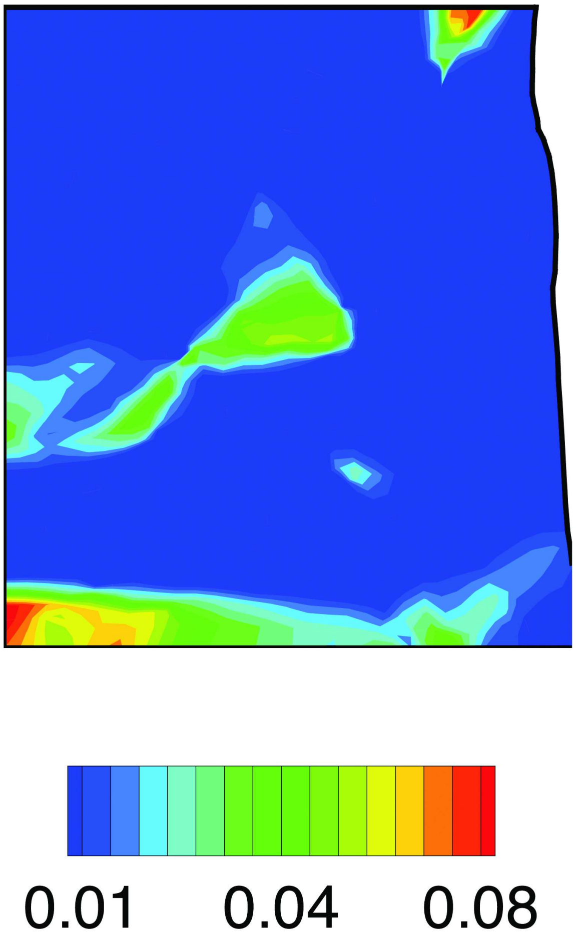

Fig 13b
83x134mm (600 x 600 DPI)

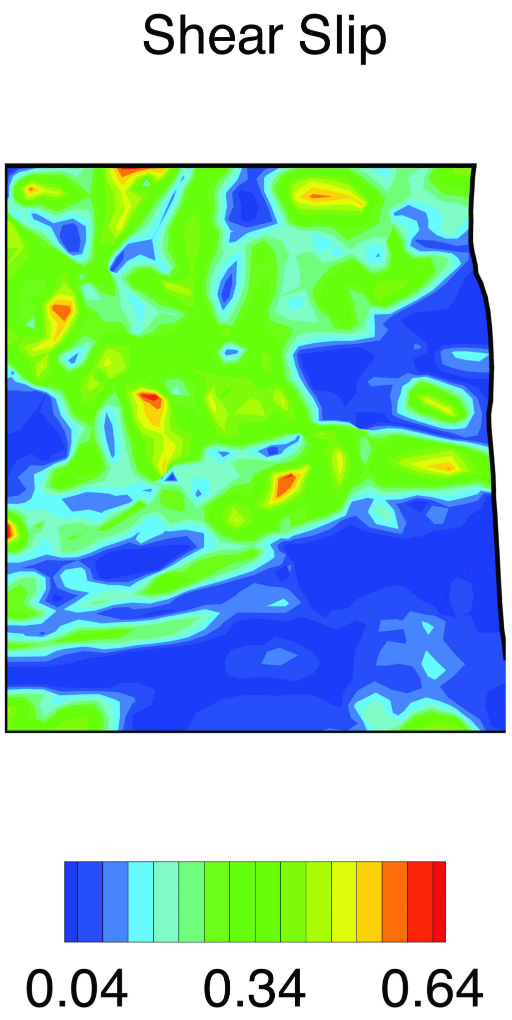

Fig 14a
83x153mm (600 x 600 DPI)

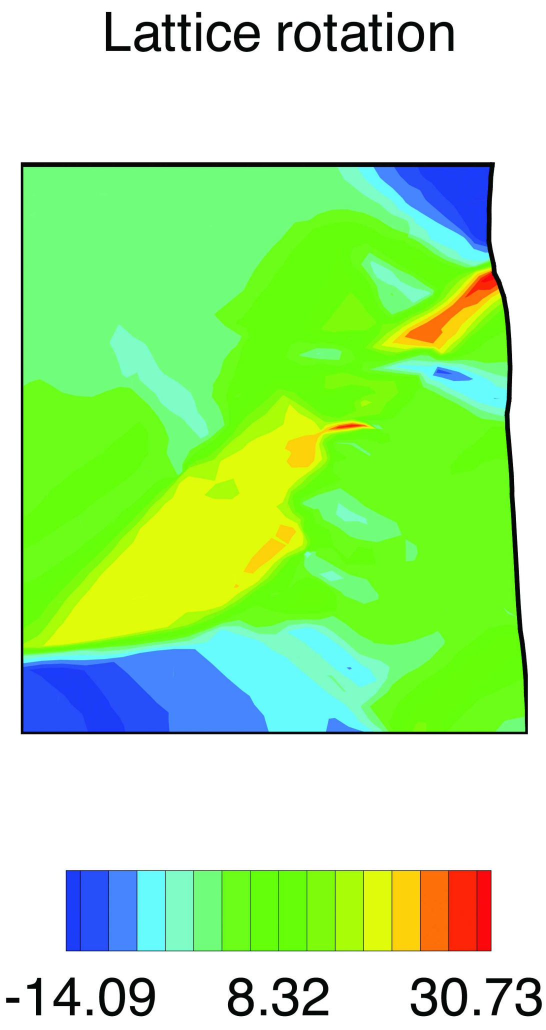

Fig 14b
83x153mm (600 x 600 DPI)

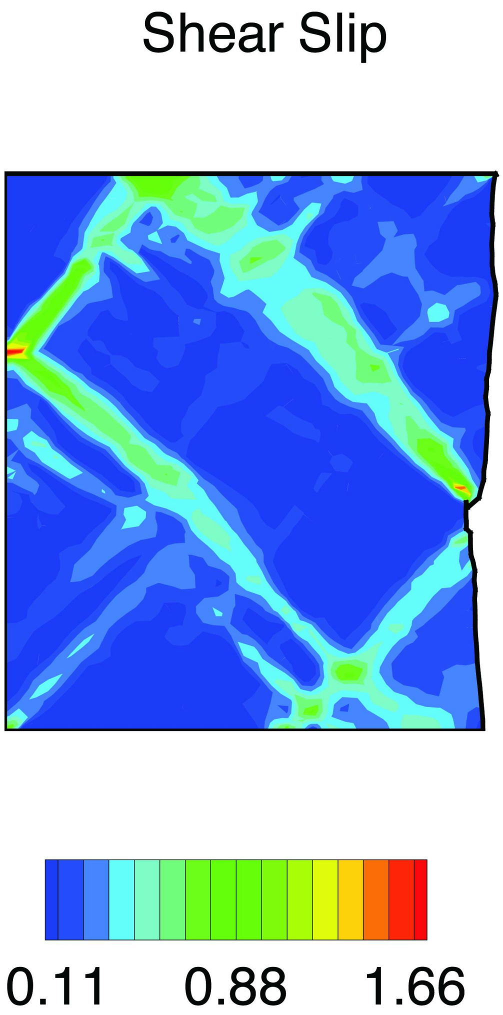

Fig 15a
83x148mm (600 x 600 DPI)

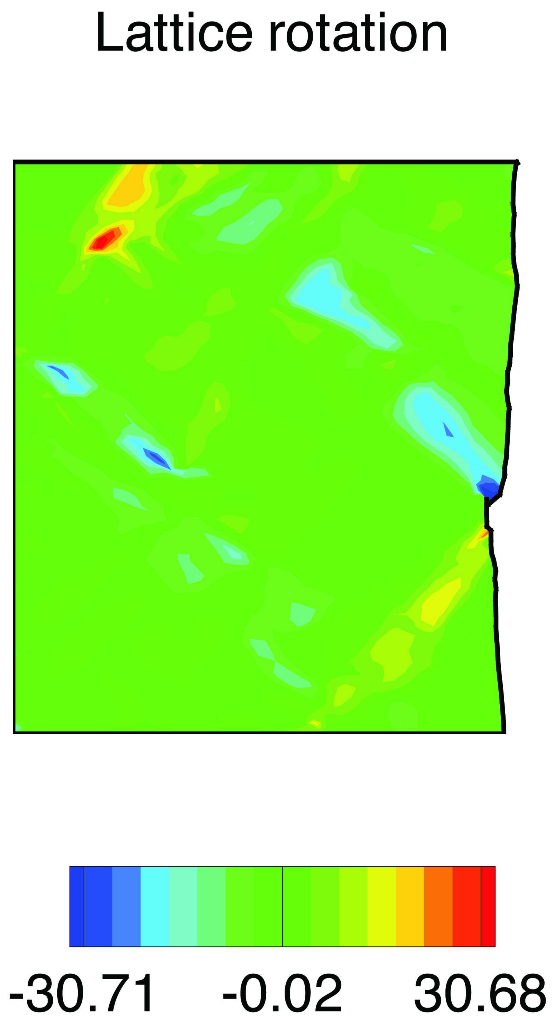

Fig 15b
83x148mm (600 x 600 DPI)

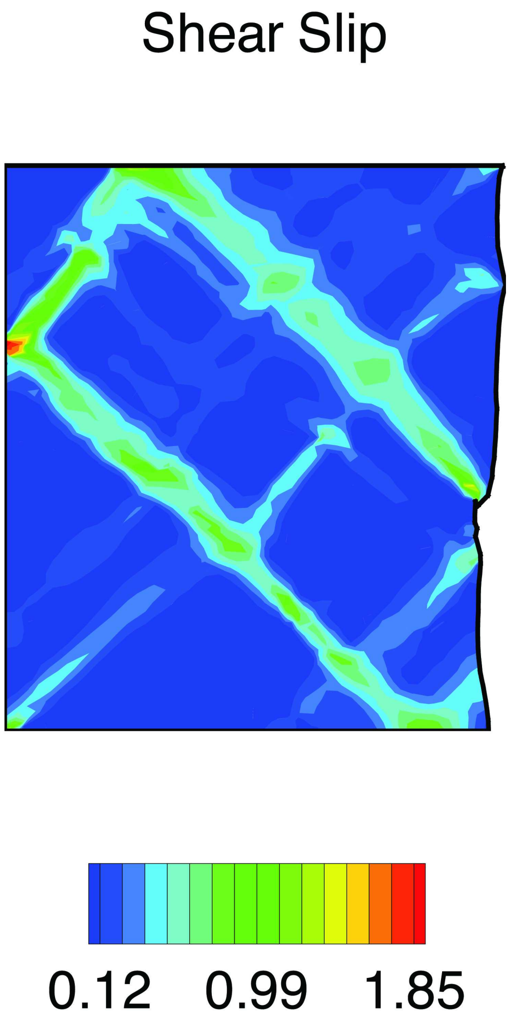

Fig 15c
83x148mm (600 x 600 DPI)

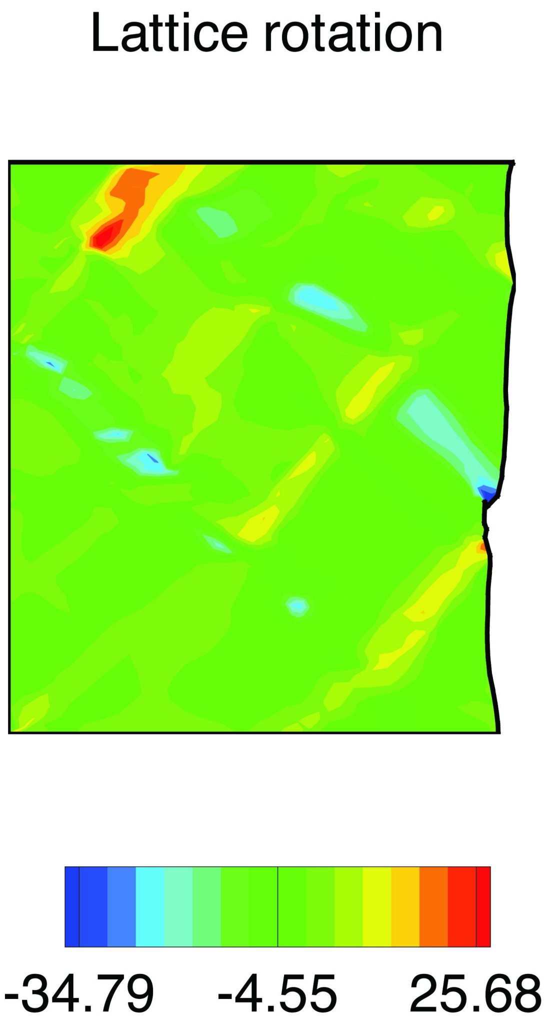

Fig 15d
83x148mm (600 x 600 DPI)

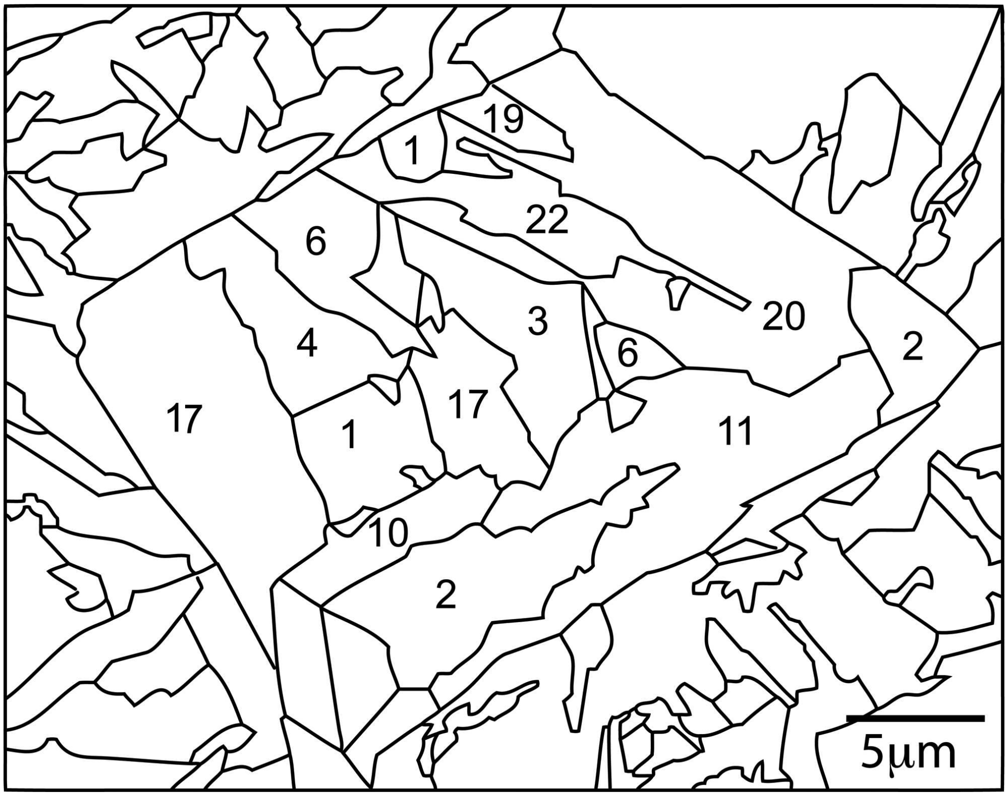

Fig 16
83x66mm (600 x 600 DPI)

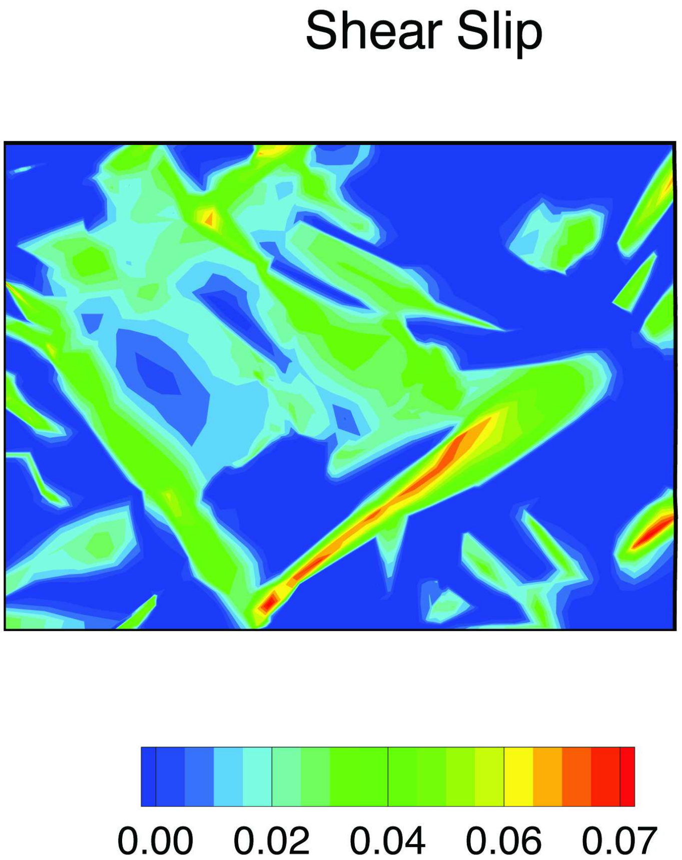

Fig 17a
83x83mm (600 x 600 DPI)

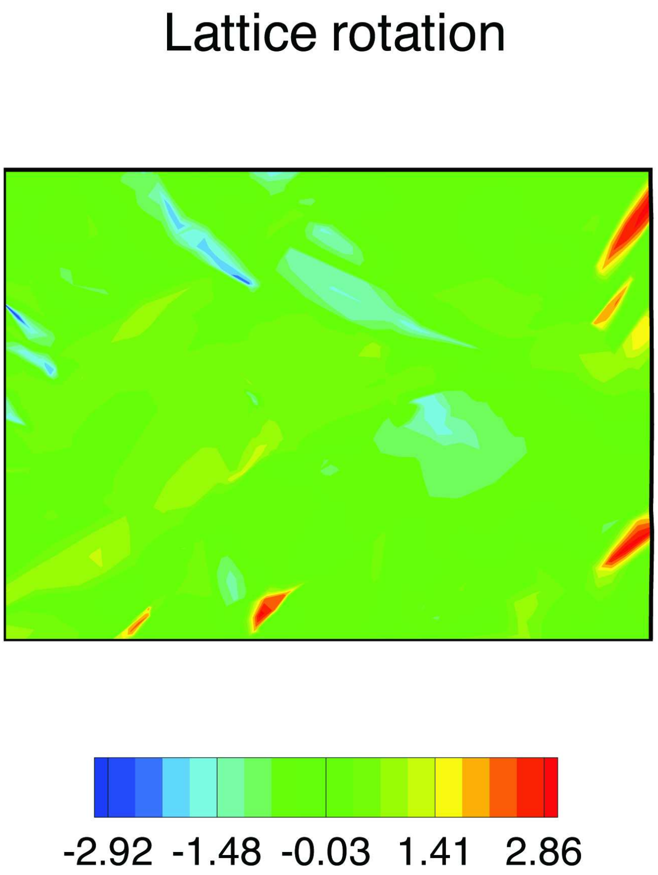

Fig 17b
83x83mm (600 x 600 DPI)

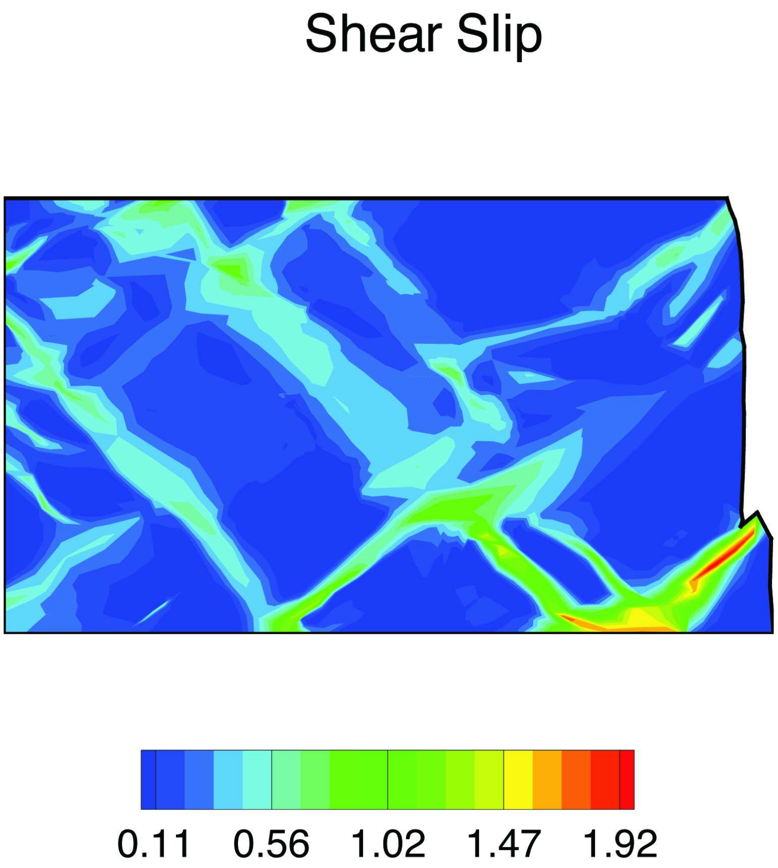

Fig 17c
83x83mm (600 x 600 DPI)

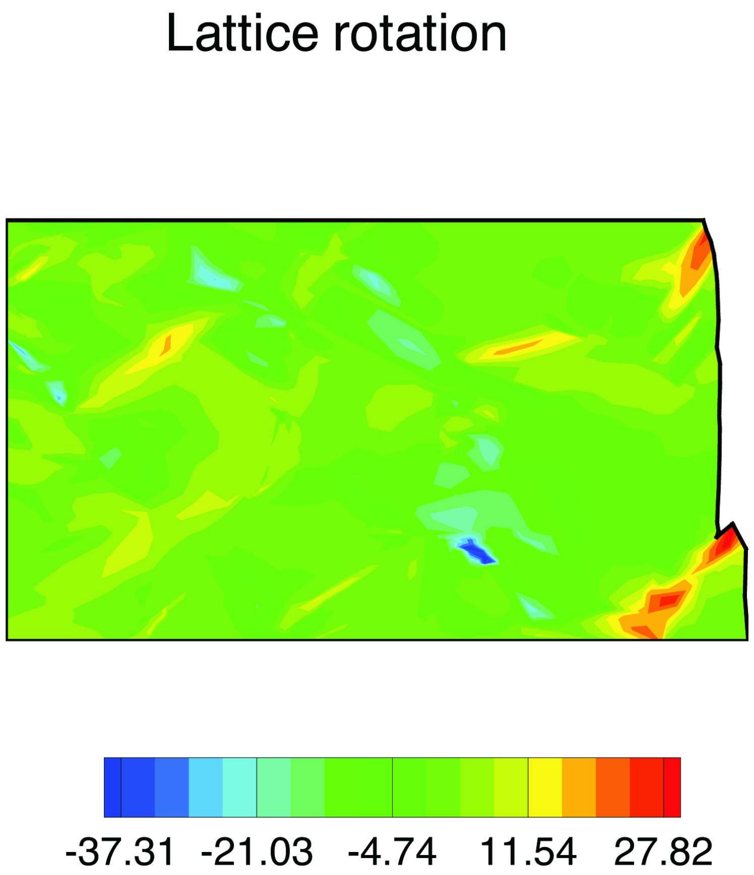

Fig 17d
83x83mm (600 x 600 DPI)

List of Tables

Table 1: The 24 variants corresponding to K-S OR and their numbering
Table 2: Properties of martensitic and austenitic grains, isotropic elasticity have been assumed

List of Figures

Figure 1. Variant alignments, three main relations can be identified: flat, sharp, and extended inward.

Figure 2. Lath martensite hierarchical microstructure for four scale architecture; parent austenite grains, packets, blocks, and laths.

Figure 3. Proposed L_∞ Voronoi tessellations (a) ordinary Voronoi tessellations. (b) L_∞ Voronoi tessellations to the same set of points. (c) Applying the same algorithm with tilt angle of 30^o. (d) modified L_∞ Voronoi tessellation algorithms (no sharp corners).

Figure 4. Microstructural model used in the current study, the distribution of variants in blocks and packets (variants numbered as indicated in Table 1), and loading, geometry, and boundary conditions.

Figure 5. Global stress-strain curve for experimental and predicted results for low nickel martensitic steel (Stresses values are normalized by the static yield stress).

Figure 6. Global stress-strain curve for experimental results for low nickel martensitic steel, compared with numerical results obtained using ordinary Voronoi algorithms and proposed L_∞ Voronoi algorithm.

Figure 7. Normalized mobile dislocation-densities for most active slip-systems; (a) slip-system $(\bar{1}12)/[1\bar{1}1]$, (b) slip-system $(112)/[11\bar{1}]$, and (c) slip-system $(1\bar{1}2)/[\bar{1}11]$ at a nominal strain of 15%. Values normalized by mobile dislocation-densities saturation values, $\rho_{m,s}^{(\alpha)} = 6.86 \times 10^{14} m^{-2}$.

Figure 8. Normalized immobile dislocation-densities for most active slip-systems; (a) slip-system $(\bar{1}12)/[1\bar{1}1]$, (b) slip-system $(112)/[11\bar{1}]$, and (c) slip-system $(1\bar{1}2)/[\bar{1}11]$ at a nominal strain of 15%. Values normalized by immobile dislocation-densities saturation values, $\rho_{im,s}^{(\alpha)} = 1.16 \times 10^{16} m^{-2}$.

Figure 9. Results obtained for the modelled specimen, at a nominal strain of 15% (a) Shear slip contours γ, (b) schematic of the specimen with shear localization region highlighted.

Figure 10. $[010]_\gamma$ stereographic projection for variant #11 slip-systems relative to the loading direction, the locus of maximum resolved shear stress (the inner circle) and the long direction of the variants (presented as * in figure a) (a) the slip directions, (b) the slip planes.

Figure 11. Results obtained for the modelled specimen, at a nominal strain of 15%; (a) lattice rotation in degrees; (b) normalized normal stresses; (c) normalized shear stresses. Stresses values are normalized by the static yield stress.

Figure 12. Normalized mobile dislocation-densities for most active slip-systems for $[011]_\gamma$ loading direction; (a) slip-system $(011)/[11\bar{1}]$, (b) slip-system $(011)/[1\bar{1}1]$, at a nominal strain of 15%.

Figure 13. Normalized immobile dislocation-densities for most active slip-systems for $[011]_\gamma$ loading direction, (a) slip-system $(011)/[11\bar{1}]$, (b) slip-system $(011)/[1\bar{1}1]$, at a nominal strain of 15%.

Figure 14. Results obtained for the modelled specimen for $[011]_\gamma$ loading direction, at a nominal strain of 15%, (a) shear slip γ, (b) lattice rotation in degrees.

Figure 15. Results obtained for the modelled specimen with 10% of retained austenite, at a nominal strain of 15%. (a) shear slip γ, (b) lattice rotation in degrees, both for retained austenite placed inside the blocks (Model 1). (c) shear slip γ, (d) lattice rotation in degrees, both for retained austenite placed at block boundary (Model 2).

Figure 16. Physically representative microstructure mapped from SEM/EBSD steel microstructure and the distribution of variants [41].

Figure 17. Results obtained from mapped experimental specimens, at nominal strains of 5% and 15%. (a) shear slip γ, (b) lattice rotation in degrees, both at nominal strain of 5%. (c) shear slip γ, (d) lattice rotation in degrees, both at a nominal strain of 15